Acta Geochim (2025) 44:1308–1327
https://doi.org/10.1007/s11631-025-00793-8

ORIGINAL ARTICLE

Deep geological processes of the early Middle Jurassic granitic complexes in the Songjianghe area, Jiapigou-Haigou collage zone, Northeast China: Evidence from zircon U–Pb dating, elemental geochemistry and Sr–Nd–Hf isotopes

Xinwen Zhang[1] · Jinggui Sun[1] · Zuochao Lin[2] · Shu Wang[1] · Yunpeng He[1]

Received: 11 March 2025 / Revised: 12 May 2025 / Accepted: 21 May 2025 / Published online: 2 July 2025

Abstract The deep geologic processes between the Xing'an-Mongolian Orogenic Belt and the North China Craton in the Mesozoic are crucial to reveal the magmatic and tectonic evolution and their constraints on mineralization in the Jiapigou-Haigou collage zone. In this paper, We have presented the geochronology, geochemistry and Sr–Nd–Hf isotopic compositions of the Middle Jurassic granitic complexes in the Songjianghe area, Jilin Province. The granitic complexes can be categorized into four groups based on their geologic characteristics, with corresponding zircon U–Pb isotope ages of 177 Ma, 172 Ma, 169 Ma and 168–167 Ma, respectively. These granitoids exhibit calc-alkaline to high-K calc-alkaline, metaluminous to weakly peraluminous I-type characteristics, which show relative enrichment in LILEs (Rb, Sr, Ba) and depletion in HFSEs (Nb, Zr). Geochemical analyses reveal high initial $^{87}Sr/^{86}Sr$ ratios of 0.70633–0.70740, coupled with low εNd(t) values ranging from −10.65 to −13.23. The zircon analyses show similarly negative εHf(t) values ranging from −16.9 to −3.2. The integrated elemental and Hf–Sr–Nd isotopic signatures demonstrate that the primitive magmas of the four group rocks were primarily derived from partial melting of thickened Archean lower crust, with the exception of the Group IV rocks, which exhibit significant evidence of crustal contamination. The residual mineral assemblages during the magma-forming process varied from amphibole to eclogite facies. These findings indicate that magmatism in the Songjianghe region likely resulted from the accretion and delamination of the Archean crust in the collage zone during the subduction of the Paleo-Pacific Plate beneath the Eurasian continent.

Keywords U–Pb datings · Elemental geochemistry and Sr–Nd–Hf isotopes · Petrogenesis · Middle Jurassic granitic complexes · Deep geologic processes · Songjianghe area

1 Introduction

Granite constitutes a fundamental component of the Earth's continental crust and represents one of the most significant products of continental crustal growth and evolution (Chappell and White 1992). As a direct manifestation of deep earth processes and crustal contamination, granitic magmatism preserves crucial information on the origin of the magma and deep geologic events occuring during magma evolution (Brown and Fyfe 1970; Whitney and Northrop 1988; DePaolo et al. 1992; Pitcher 1997; Wu et al. 2011). The petrogenesis of granitoids that formed in orogenic and plate boundary collage zones is notably more complex than that of intraplate anorogenic magmatic rocks. These granitic rocks represent the products of continued collisional orogenic processes and record the tectonic transition to intraplate anorogenic environments (Sylvester 1998; Liegeios et al. 1998).

Substantial progress has been made in understanding the petrogenesis and geodynamic background of the Phanerozoic granites in northeastern China. Investigation of the Mesozoic granite belt in the Lesser Xing'an-Zhangguangcai

Supplementary Information The online version contains supplementary material available at https://doi.org/10.1007/s11631-025-00793-8.

✉ Jinggui Sun
sunjinggui@jlu.edu.cn

[1] College of Earth Science, Jilin University, Changchun 130061, China

[2] Team 604, Jilin Nonferrous Metals Geological Exploration Bureau, Jilin, China

Ranges have revealed that the Early and Middle Jurassic granitoids can be chronologically divided into four periods as follows: (1) Early Jurassic (> 175 Ma), characterized by magma derived from the partial melting of thickened lithosphere during the subduction of the Paleo-Pacific plate, contributing to the thickening of the lithosphere and accelerating the mixing of juvenile crust and ancient crust (Wu et al. 2003, 1999; Han et al. 1998); (2) early Middle Jurassic (~ 172 Ma), the collision orogeny between the Jiamusi Plate and the western Zhangguangcai Massif likely resulted in the formation of biotite monzogranite; (3) middle Middle Jurassic (~ 168 Ma), the subduction of the oceanic plate persisted, producing crust-mantle mixing magmas; (4) late Middle Jurassic (162–165 Ma), representing the tectonic setting transition from compressional orogeny to postorogenic extensional environment (Wu et al. 1999; Liang et al. 2015). The Early and Middle Jurassic granites in Yanbian exhibit similar characteristics (Zhang et al. 2004). Recent studies suggest that the formation of the Early Jurassic granites in central Yanbian coincided with the crust-mantle mixing process at the continental margin under the subduction of the Paleo-Pacific Plate underneath the Eurasian continent (Zhang et al. 2023).

In recent decades, research on late Mesozoic magmatism and geodynamic processes in the collage zone between the northern margin of the NCC (North China Craton) and the CAOB (Central Asian Orogenic Belt) has received considerable attention (Han et al. 1998; Liu et al. 2002; Deng et al. 2014; Li et al. 2017). Tectonically, the Songjianghe area occupies a central location in the Jiapigou-Haigou collage zone between the NCC and the Xing'an-Mongolian Orogenic Belt (XMOB). Meanwhile, the study area is a world-famous gold metallogenic belt with large-scale mineralization occurring at 180–174 Ma (Han et al. 2022), including the Songjianghe gold deposit (154 Ma) (Zhang et al. 2019) and the Haigou gold deposit (163–161 Ma) (Li et al. 2017). The Songjianghe area is an ideal region for investigating the deep geologic processes in the collage zone triggered by the subduction of the Paleo-Pacific Ocean beneath the Eurasian continent since the Mesozoic (Fig. 1a). Recent studies indicate that the Mesozoic granites in the eastern sector of the XMOB primarily formed in the Early-Middle Jurassic (Wu et al. 2003; Zhang et al. 2002, 2004; Yang et al. 2018; Han et al. 2019), with their low initial Sr and high Nd isotope values suggesting that the magma originated predominantly from the juvenile crust. Previous investigations of granites in the Songjianghe area have identified the extensive Middle Jurassic plutons, including the Dapuchaihe pluton (165–162 Ma) and the Huangnihe pluton (168–153 Ma) (Zhang et al. 2002; Deng et al. 2014). Based on the detailed investigation of the granitic complex exposed in the study area (Fig. 1c), we systematically carried out zircon U–Pb dating, elemental geochemistry and Sr–Nd–Hf isotope analyses. These investigations provide insights into early Middle Jurassic magmatism and geodynamic background, offering fundamental theoretical support for further research on the deep geologic processes of the Jiapigou-Haigou collage zone and their constraints on Au mineralization.

2 Regional geology and granitic complexes

The study area is located in the central part of the Jiapigou-Haigou collage zone on the edge of northeastern China. From a tectonic perspective, this indicates an active continental margin tectonic environment under the Paleo-Pacific Ocean subduction beneath the Eurasian continent since the Mesozoic (Fig. 1a). Regional geologic studies have revealed that the dominant tectonic structure in the study region is the NE-trending Huifahe supracrustal transform fault, which represents the southern sector of the Dunhua-Mishan Fault. Additional significant faults include the NWW-trending Fu'erhe, Jinyinbei and Jiapigou and the NE-trending Ji'an-Songjiang Fault (Fig. 1b). The strata exposed in the southern section of the pre-Mesozoic Jinyinbei Faults consist of granitic gneisses and supracrustal rocks, and the study area is characterized by the pre-Mesozoic metamorphic facies and Paleozoic granites. Since the Mesozoic, the Songjianghe area has developed voluminous granitic complexes and continental volcanic-sedimentary rocks within the Mesozoic basin, with large-scale Cenozoic basalts distributed in the southern part of the study region (Fig. 1c). Investigations of granitic intrusive rocks reveal that Paleoproterozoic intrusive tonalite-trondhjemite-granodiorite (TTG) rocks are sporadically exposed, with the rock assemblage comprising gabbro, granodiorite and monzogranite (Chen et al. 2013; Yu et al. 2021). The Mesozoic intrusive rocks are widely distributed (Fig. 1c), and primary lithofacies are gabbro, diorite, granodiorite, monzogranite and quartz diorite. These rocks can be subdivided into six periods: Early Triassic, Late Triassic, Early Jurassic, Middle Jurassic, Late Jurassic and Early Cretaceous (Sun et al. 2008). The study area has experienced significant geologic processes, including Archaen cratonization, the formation of the XMOB and the Indo-Chinese and Yanshanian orogenic events. In terms of mineralization, the Cu-Ni sulfide mineralization is genetically associated with the Late Triassic basaltic-ultramafic intrusive rocks distributed in the northern sector of the collage zone between the XMOB and the NCC. The Au and Cu-Mo polymetallic mineralizations are closely related to early-Middle Jurassic and Early Cretaceous granitic complexes (Sun et al. 2012, 2013). The Jiapigou-Haigou collage zone represents a significant gold mineralization belt in northeastern China (Deng et al. 2014),

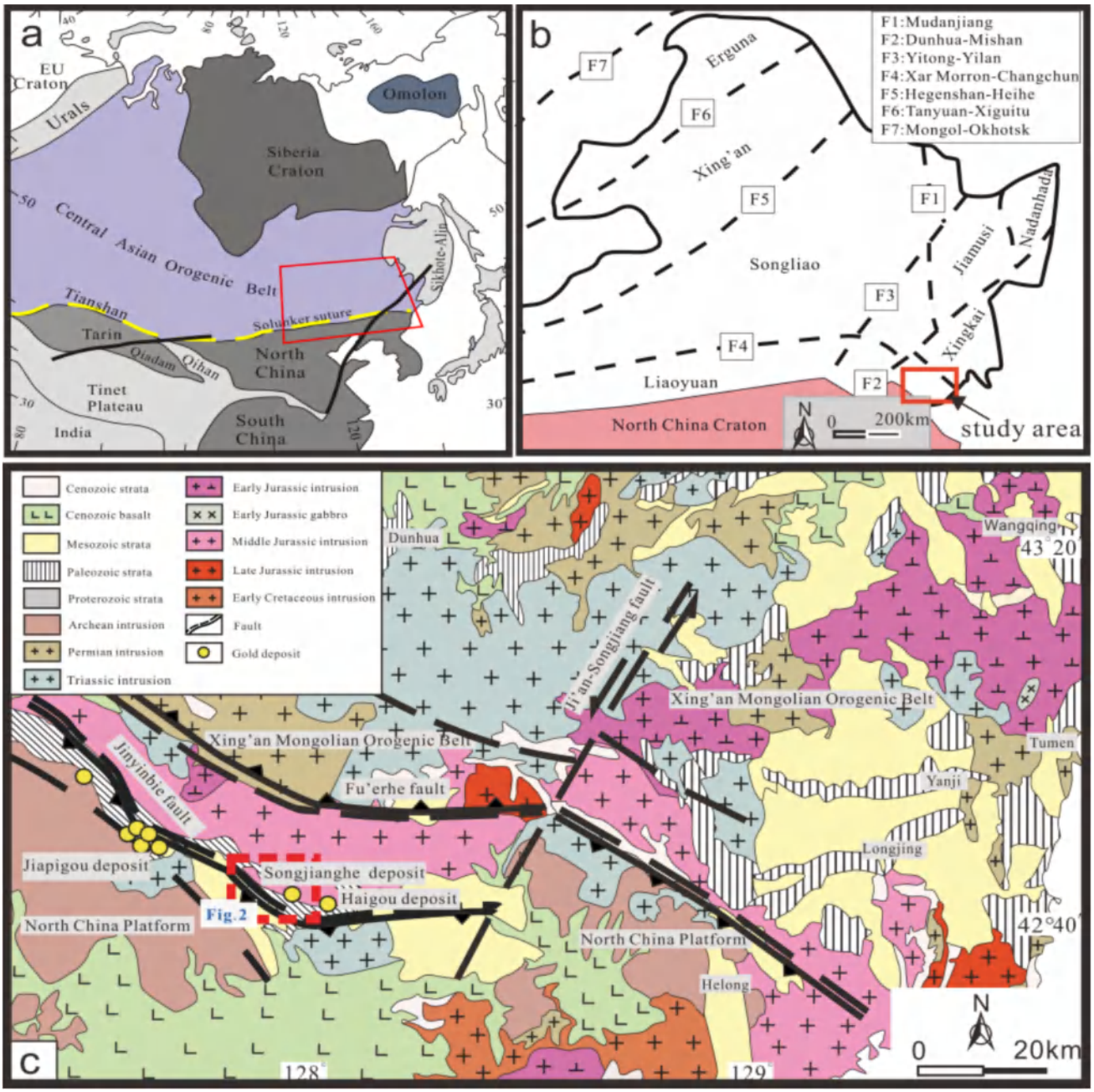

Fig. 1 Geotectonic location of the study area and regional geologic map [modified from Jilin Geological Journal, 2022 (Revised)]

with widely distributed early-Middle Jurassic granitic complexes in the northern part, which mainly consist of granodiorite and diorite, while Indo-Chinese granites are exposed in the southern region. This study revealed that the granitic complexes exposed in the Songjianghe area are predominantly syenogranite and monzogranite on the basis of geologic mapping (Fig. 2). These rocks can be further subdivided into massive medium-grained syenogranite (177 Ma), gneissic diorite, granodiorite and massive quartz monzonite (172 Ma), porphyritic medium-grained syenogranite (169 Ma) and massive medium-grained syenogranite and monzogranite (168–167 Ma). Numerous weakly gneissic medium- and fine-grained syenogranites are exposed in the eastern part of the study area, while in the medium- and fine-grained syenogranite, monzogranite occurs in the central and northern sector. Porphyritic medium-grained syenogranite is located proximal to the Songjianghe Fault. The gneissic diorite and granodiorite are located in the northeast, and massive quartz monzonite is located in the southern region, where it intruded the

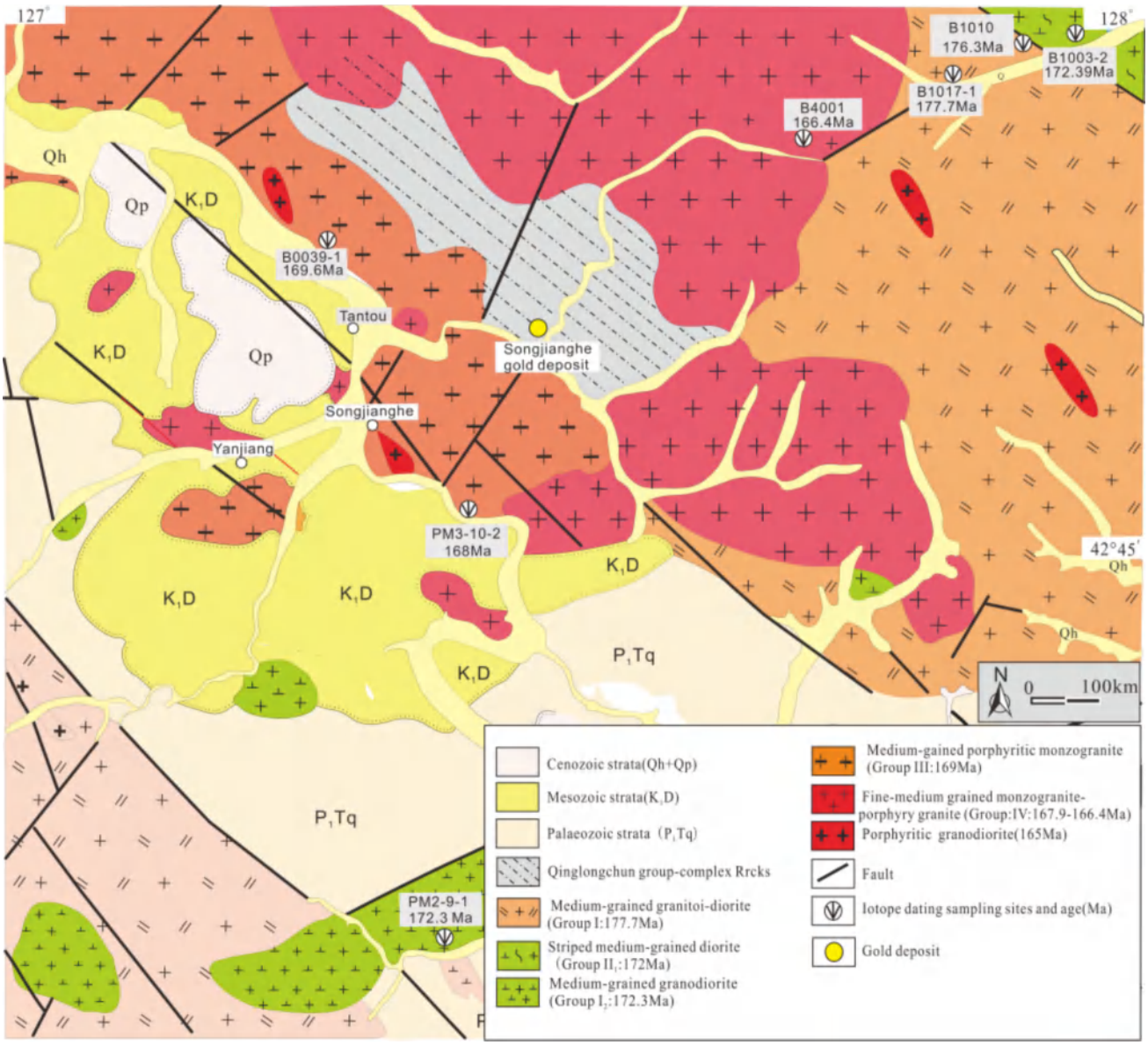

Fig. 2 Detailed geology and lithofacies distribution of the Songjianghe granitic complex, showing the sample locations (1:50000 Mineral Geologic Survey, 2018 revision)

Indo-Chinese granite as an irregular intrusion (Fig. 2). The petrographic characteristics of these rocks are illustrated in Fig. 3 and Supp 1.

3 Sampling and analytical methods

Based on careful field observations and laser Raman mineralogy identification, representative samples were selected for corresponding chronologic, major and trace elements and Sr–Nd–Hf isotope analyses.

3.1 Zircon U–Pb dating

Sample processing and zircon separation were carried out by the Regional Geological Survey of Hebei Province, China. The U–Pb geochronology of zircons was performed via laser ablation inductively coupled plasma mass spectrometry (LA-ICP-MS) at the Key Laboratory of Northeast Asia Mineral Resource Evaluation, Ministry of Land and Resources of China, Jilin University. The analysis instrument consists of a quadrupole ICP-MS (Agilent 7900) coupled to a 193-nm ArF excimer laser (COMPexPro 102, Coherent, DE) and an automated positioning system. During the analyses, the laser spot size

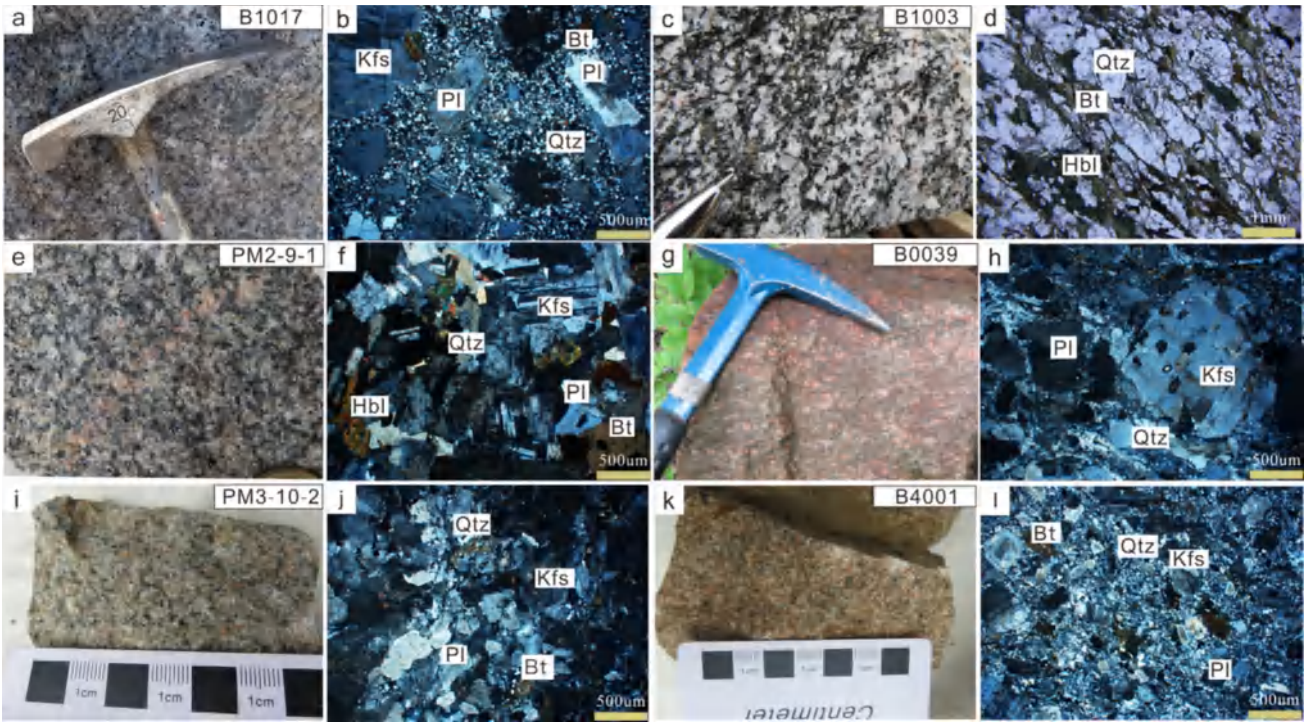

Fig. 3 Petrographic and microscopic characteristics of zircon U–Pb isotope dating samples in the study area. **a** The massive syenogranite facies (Group I). **c** The gneissic diorite facies (Group II) **e** Massive quartz monzonite (Group II). **g** Porphiritic syenogranite (Group III). **i** Massive syenogranite (Group IV). **k** Massive monzogranite (Group IV). Microscopic-scale petrographic characteristics of the Songjianghe granitic complex (**b, d, f, h, j** and **l**). Mineral abbreviations: Pl = plagioclase, Qtz = quartz, Hbl = hornblende, Kfs = K-feldspar, Bt = biotite

was 32 μm, the energy density was 10 J/cm^2, and the repetition frequency was 8 Hz. Concordant ages and graphs were obtained using Isoplot/Ex (3.0). Pb was corrected using LA-ICP-MS Pb correction (version 3.15) following Andersen's method. The analyzed data are presented as U–Pb concordia plots with a 2σ error.

3.2 Major and trace element analyses

The major element compositions were analyzed with x-ray fluorescence (XRF) with an analytical uncertainty (1%–3%) at the Langfang Regional Geological Survey, Hebei Province, China. Trace element measurements were performed with an Agilent 7500a ICP-MS instrument. For each analysis, approximately 60 mg of crushed whole rock powder was first dissolved in HF/HNO_3 (10:1) and then placed in a beaker at 100 °C for 6 days. After dissolution, the mixture was evaporated to dryness, refluxed in 7 N HNO_3 and then dried again. The dried sample was then dissolved in 2% HNO_3 until the ratio of sample-to-solution weight reached 1:1000. Based on standard determinations, trace elements are generally analyzed with a precision > 10%.

3.3 Sr–Nd-Hf isotope analysis

Hf isotope analysis was performed at the State Key Laboratory for Mineral Deposits Research, Nanjing University, with a Neptune multi-collection ICP-MS instrument. The analyses were performed primarily at a 35-lm beam diameter and 8-Hz repetition frequency. The instrumental conditions and data acquisition procedures were similar to those described by Wu et al. (2006). Atomic masses of 172, 173, 175 to 180 and 182 were measured simultaneously in static collection mode. The reference zircon Mud Tank ($^{176}Hf/^{177}Hf = 0.282507 \pm 6$) and the standard zircon 91,500 were used to monitor performance conditions and analytical accuracy (Woodhead and Hergt 2005; Scherer et al. 2001). Initial Hf values were calculated using a ^{176}Lu value with a decay constant of 1.865×10^{-11} per year and chondrite models of $^{176}Hf/^{177}Hf = 0.282772$ and $^{176}Lu/^{177}Hf = 0.0332$. The depleted mantle Hf model age (TDM) was calculated using measured zircon $^{176}Lu/^{177}Hf$ ratios, and the depleted mantle model had a $^{176}Hf/^{177}Hf$ ratio of 0.28325, similar to the mid-ocean ridge basalt (MORB) mean value of $^{176}Lu/^{177}Hf = 0.0384$, and a mean crustal (CC) ratio of – 0.55 (Nowell et al. 1998; Griffin et al. 2000, 2002). All isotope results are reported with 2σ uncertainties.

The in situ Sr–Nd isotopic composition was determined by isotope dilution method. The measurements were carried out at Guizhou Tongwei Analytical Technology Co., Ltd. A thermal ionization mass spectrometer (TIMS) was used in the experiments. All the Sr data were corrected by mass fractionation to $^{86}Sr/^{87}Sr = 0.1194$ and reported relative to the NBS-987 standard value of $^{87}Sr/^{86}\ Sr = 0.710222 \pm 20$ (2σ). For the Nd isotope analysis, $^{146}Nd/^{144}Nd = 0.7219$ was used as a standard for mass fractionation correction, and the Nd isotope ratios were normalized to the Ames value $^{143}\ Nd/^{144}\ Nd = 0.511966 \pm 16$ (2σ). The $^{147}Sm/^{144}$ Nd and $^{143}Nd/^{144}$ Nd ratios of 0.1967 and 0.512638, respectively, and the average chondrite and depleted mantle ratios of 0.2137 and 0.51315, respectively, were used in the calculation of the εNd(t) values, fSm/Nd ratios and Nd model ages (Hamilton et al. 1983; Liu et al. 2019).

4 Results

4.1 Zircon U–Pb dating

Group I: massive syenogranite (B1017)

The zircon grains are euhedral to subhedral, with length-width ratios ranging from 2.5 to 4.0. The grains show typical oscillatory growth zoning in the cathodoluminescence (CL) images, exhibiting magmatic zircon characteristics (Belousova et al. 2002). The $^{206}Pb/^{238}U$ ages of the analyzed zircons range from 174 to 183 Ma, with a weighted mean age of $^{206}Pb/^{238}U = 177.7 \pm 1.3$ Ma (MSWD = 0.44, n = 18) (Supp 2, Fig. 4).

Group II: gneissic diorite, quartz monzonite (B1003, PM2-9-1).

Gneissic diorite (B1003): The zircon grains are euhedral to subhedral, with length-width ratios ranging from 2.5 to 4.5. Zircon grains show typical oscillatory growth zoning in the CL images, which is characteristic of magmatic zircons. The $^{206}Pb/^{238}U$ ages of the analyzed zircons range from 169 to 178 Ma, yielding a weighted mean age of $^{206}Pb/^{238}U = 172.4 \pm 0.9$ Ma (MSWD = 1.09, n = 18) (Supp 2, Fig. 4).

Quartz monzonite (PM2-9–1): The zircon grains are euhedral to subhedral, with a length-width ratio of 1.0–3.5. The zircon grains show typical oscillatory growth zoning in the CL images (Fig. 4C), which indicates a magmatic origin. The $^{206}Pb/^{238}U$ ages of the analyzed zircons range from 166 to 174 Ma, with a weighted mean age of $^{206}Pb/^{238}U = 172.3 \pm 1.2$ Ma (MSWD = 0.84, n = 16) (Supp 2, Fig. 4).

Group III: Porphyritic medium-grained syenogranite (B0039).

The zircon grains are euhedral to subhedral, with length-width ratios of 3.0–5.0. These grains show typical oscillatory growth zoning in the CL images, exhibiting magmatic zircon characteristics. The $^{206}Pb/^{238}U$ ages of the analyzed zircons range from 167 to 173 Ma, with a weighted mean age of $^{206}Pb/^{238}U = 169.6 \pm 1.8$ Ma (MSWD = 1.3, $n = 9$) (Supp 2, Fig. 4).

Group IV: Medium-grained syenogranite, fine-grained monzogranite (PM3-10–2, B4001).

Medium-grained syenogranite (PM3-10–2): The zircon grains are euhedral to subhedral, with length-width ratios ranging from 1.0 to 2.5. The grains show typical well-oscillating growth zoning in the CL images (Fig. 4E). The U and Th concentrations are 266–789 ppm and 106–719 ppm, respectively, with U/Th = 0.40–0.91, indicating that they are magmatic zircons. The $^{206}Pb/^{238}U$ ages of the analyzed zircons range between 164 and 171 Ma, yeilding a weighted mean age of $^{206}Pb/^{238}U = 167.9 \pm 1.1$ Ma (MSWD = 0.68, $n = 14$) (Supp 2, Fig. 4).

Fine-grained monzogranite (B4001): The zircon grains are euhedral to subhedral, with length-width ratios of 2.0–3.5. The grains show good oscillating growth zoning in the CL images (Fig. 4F). The contents of U and Th are 34–1198 ppm and 19–244 ppm, respectively. The Th/U ratios of 0.10–0.80 indicate that they are magmatic zircons. The $^{206}Pb/^{238}U$ ages of the analyzed zircons range from 162 to 171 Ma, with a weighted mean age of $^{206}Pb/^{238}U = 166.4 \pm 1.2$ Ma (MSWD = 1.3, n = 17) (Supp 2, Fig. 4).

4.2 Geochemistry

4.2.1 Major and trace elements

The major and trace element compositions of the above four groups of granites were analyzed in this study (Supp 3). Group I has the following composition: $SiO_2 = 68.61–69.96$ wt%, $Al_2O_{3=}14.67–15.54$ wt%, CaO = 1.81–2.12 wt%, $K_2O = 3.67–3.77$ wt%, $Na_2O + K_2O$ content of 8.14–8.34%, K_2O/Na_2O ratio of 0.82–0.85 and Mg# value of 33–37. On the TAS diagram (Fig. 5a), Group I plots near the intersection of granodiorite, granite and quartz monzonite. Group II has the following composition: $SiO_{2=}58.69–65.52$ wt%, $Al_2O_3 = 16.19–17.88$ wt%, CaO = 3.25–5.50 wt%, $K_2O = 1.66–4.18$ wt%, $Na_2O + K_2O$ content of 6.26%–8.24%, K_2O/Na_2O ratio of 0.36–1.04 and Mg# value of 40–47. On the TAS diagram, the Group II compositions plot near the intersections of diorite, granodiorite and quartz monzonite on both sides of the dividing lines. Group III has the following compositions: $SiO_{2=}68.95–73.32$ wt%, $Al_2O_{3=}13.54–15.42$ wt%, CaO = 0.93–4.16 wt%, $K_2O = 3.23–4.24$ wt%, $Na_2O + K_2O$ content of 7.57–8.93%, K_2O/Na_2O ratio of 0.62–0.97 and Mg# value of 30–39. On the TAS diagram, the Group III compositional points are distributed in the granite region. Group IV has the following

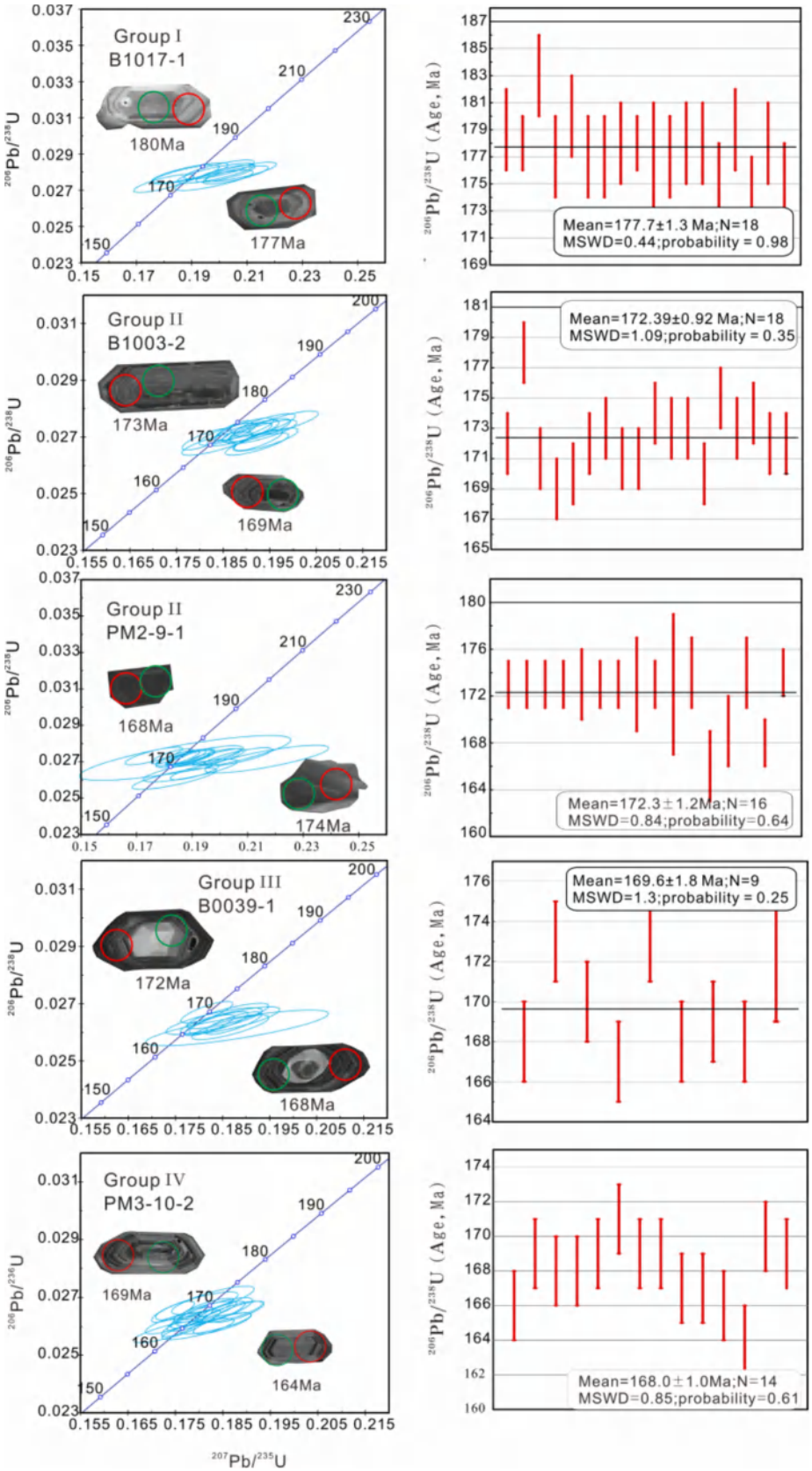

Fig. 4 Zircon U–Pb dating concordia and weighted average ages for four groups of granitic complexes (red circles, U–Pb analysis position; blue circles, Hf isotope analysis position)

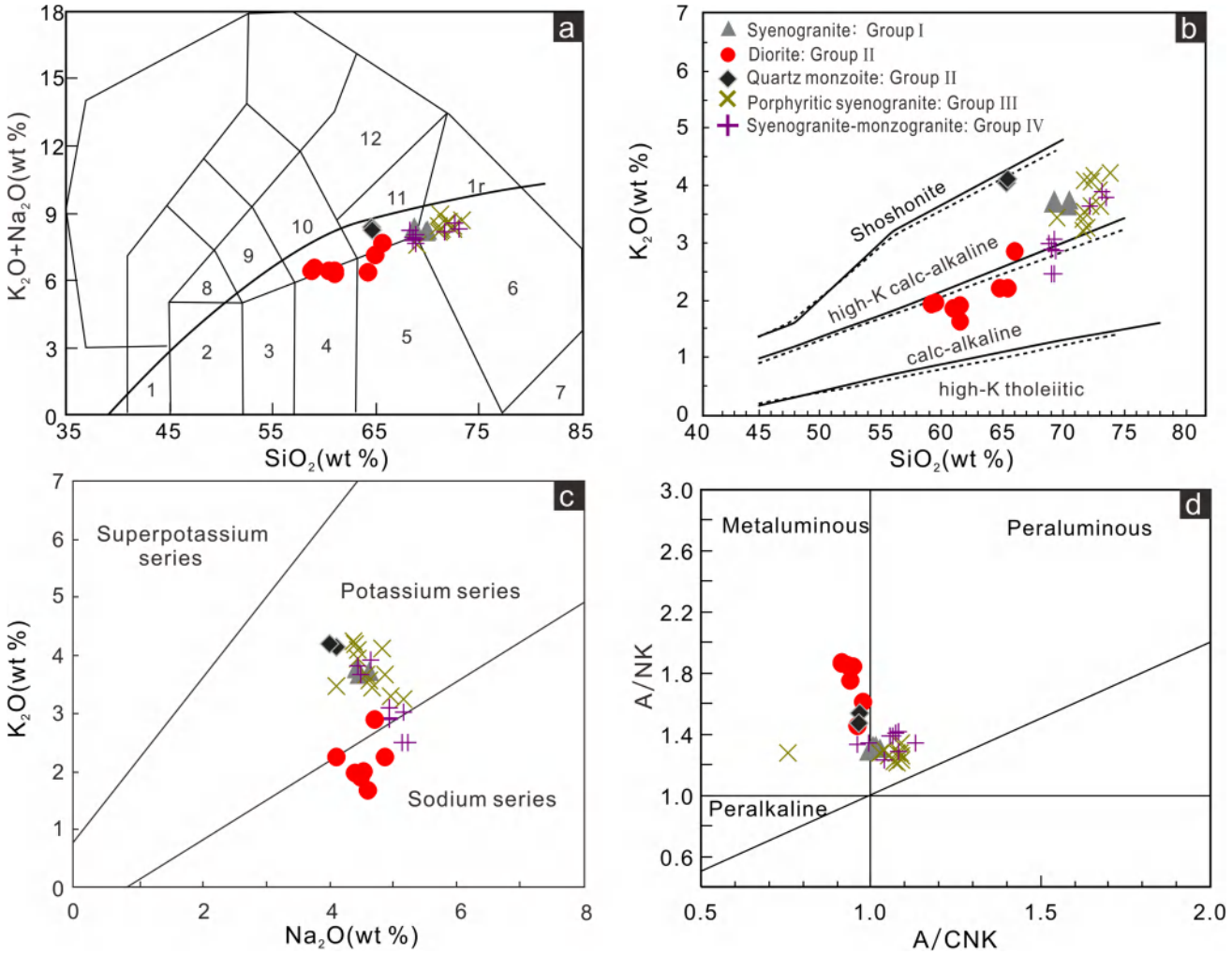

Fig. 5 **a** TAS diagram (after Middlemost 1994) Ir-Irvine dividing line with basic above and subbasic below; **b** K_2O vs. SiO_2 diagram (after Ewart 1982); **c** K_2O vs. Na_2O diagram (Peccerillo and Taylor 1976); (**d**) A/NK vs. A/CNK diagram (after Maniar and Piccoli 1989). (1) Olivine-Gabbro; (2) gabbro; (3) gabbro-diorite; (4) diorite; (5) granodiorite; (6) granite; (7) monzogranite; (8) monzogabbro; (9) monzodiorite; (10) monzonite; (11) quartzmonzonite; (12) syenite

composition: SiO_2=68.26–72.94 wt%, Al_2O_3=14.71–15.99 wt%, CaO = 1.21–2.56 wt%, K_2O = 2.48–3.91 wt%, $Na_2O + K_2O$ content of 7.63–8.55%, K_2O/Na_2O ratio of 0.47–0.86 and Mg# value of 32–39. On the TAS diagram, the Group IV compositional points plot in the granite region and near the intersections among granodiorite, granite and quartz monzonite (Fig. 5a). On the K_2O versus SiO_2 diagram, the Group I and III samples are classified as high-K calc-alkaline series; most of Group II plots in the calc-alkaline series region, with a few samples exhibiting high-K calc-alkaline affinity. The Group IV components plot on the boundary between the calc-alkaline series and the high-K calc-alkaline series and the high-K calc-alkaline series region (Fig. 5b). On the K_2O vs. Na_2O diagram, the Group I and Group III components plot in the potassic series. The Group II compositions mainly plot within the sodic series, with a minority of them plotting within the potassic series, and the Group IV components plot on the boundary between the sodic series and the potassic series (Fig. 5c). As shown in the A/NK vs. A/CNK classification diagram, Group I, Group III and Group IV belong to the peraluminous series, some of the Group I and Group IV points plot close to the metaluminous series, whereas Group II compositions show metaluminous affinity (Fig. 5d). Therefore, Group I comprises high-K calc-alkaline, potassic and weakly peraluminous facies. Group II comprises mainly calc-alkaline, sodic and partly high-K calc-alkaline, potassic and metaluminous facies. Groups III and IV comprise high-K calc-alkaline, potassic and peraluminous facies; meanwhile, Group IV exhibits high-K calc-alkaline and calc-alkaline transitional, sodic and potassic transitional peraluminous facies.

The characteristics of the rare earth elements (REEs) and trace elements revealed that the ∑REE values of Group I range from 136.85 to 143.50 ppm, with LREE/HREE ratios of 10.83 to 12.55 and δEu* values of 0.70 to 0.91. Group II has ∑REE values varying from 61.53 to 207.95 ppm, with LREE/HREE ratios of 5.21–13.90 and δEu* values of 0.69–0.94. Group III has ∑REE values ranging from 57.28 to 157.62 ppm, with LREE/HREE ratios of 13.95–27.17 and δEu* values of 0.90–1.66. Group IV has ∑REE values ranging from 94.20 to 149.69 ppm, with LREE/HREE ratios of 20.71–27.19 and δEu* values of 1.07–0.36. As shown in the chondrite-normalized REE diagram (Fig. 6a), Group I shows weakly Eu negative anomalies and a right-dipping, moderately fractionated rare earth distribution. Group II shows weakly negative Eu anomalies and a right-dipping, moderately low rare earth distribution (Fig. 6c). Group III shows weakly positive Eu anomalies and mid-high fractionation (Fig. 6e). Group IV shows weakly positive Eu anomalies and high fractionation (Fig. 6f). These results indicate that Groups III and IV experienced distinctive plagioclase fractional crystallization or residue.

The trace element analysis revealed that these rocks are enriched in large ion lithophile elements (LILEs) and depleted in high field strength elements (HFSEs). In addition, on the primitive mantle-normalized multi-element variation diagram (Fig. 6), Group I shows obvious enrichment in Rb, K, Sr, Zr

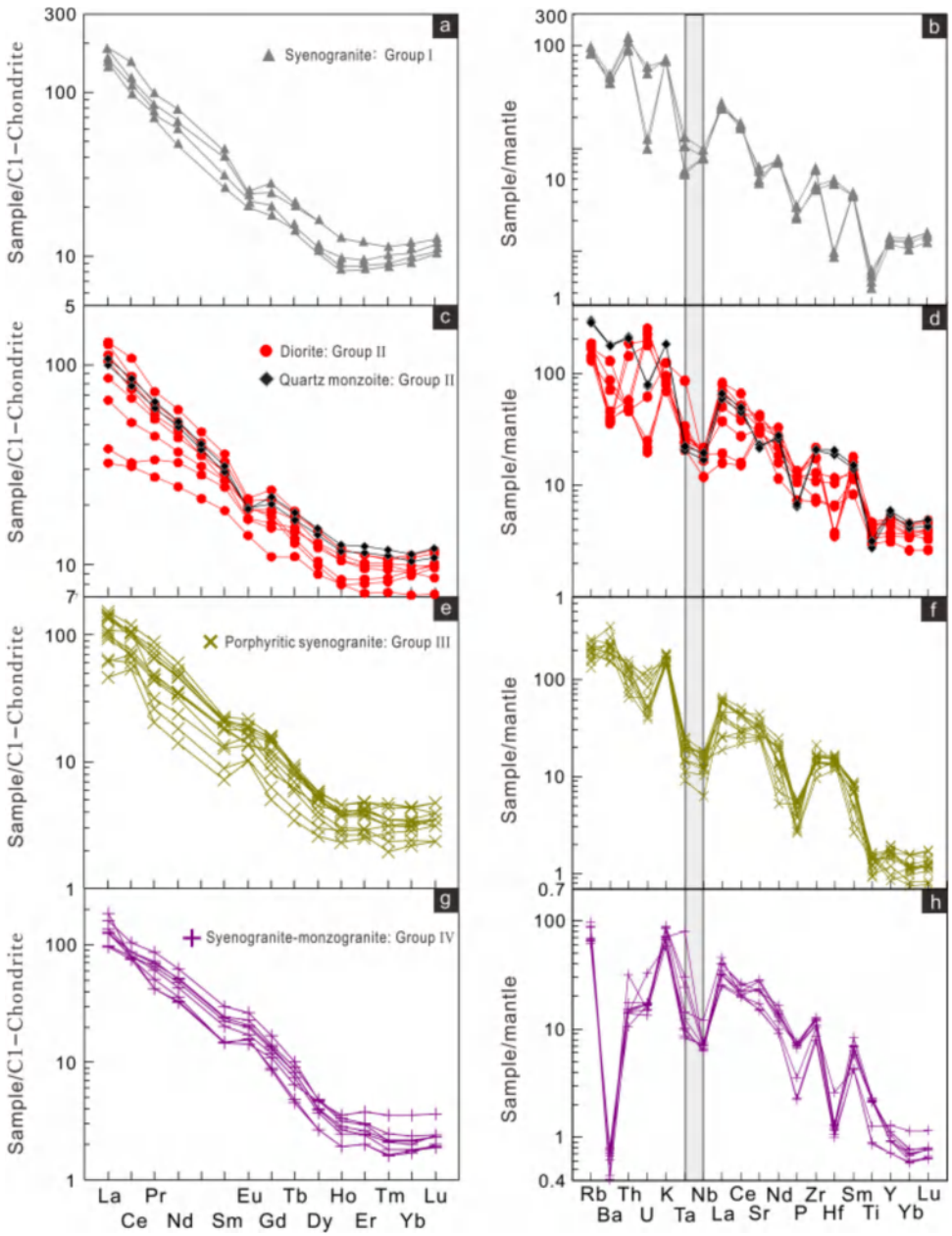

Fig. 6 **a**, **c**, **e**, **h** Chondrite-normalized REE diagram (normalized to the chondrite composition from Boynton 1984) for samples from the Songjianghe granitic complexes. **b**, **d**, **f**, **i** Primitive-mantle-normalized multi-element variation diagram (normalized to the primitive mantle composition from Sun and Mcdonough 1989)

and Sm, strong depletion in Pb and Ba and relative depletion in Th, U, Nb, Ta, Hf, Ti and P. Group II is obviously enriched in Pb, Rb, Th, U, K, Zr and Hf and relatively depleted in Ba, Nb, Ta, P and Ti. Group III has characteristics similar to those of Group II, with the difference that U, P and Ti show strong depletion. Group IV and Group I present similar trends, with differences in that Nb, Ta, Hf, Ti, Yb, Lu and Y are highly depleted.

4.2.2 Sr–Nd-Hf isotopic compositions

The Lu–Hf isotope analysis results for the representative groups of granites from the Songjianghe region are given in Supp. 4. The $^{176}Yb/^{177}Hf$ and $^{176}Lu/^{177}Hf$ ratios of the granitic complex samples range from 0.006069 to 0.050159 and 0.000310–0.001784, respectively. The $^{176}Hf/^{177}Hf$ ratios of the syenogranite sample (B1017) from Group I range from 0.282338 to 0.282923, the values of εHf(t) range from −11.8 to −9.10, and the Hf two-stage modeling age (T_{DM2}) ranges between 2.47 and 2.70 Ga. The $^{176}Hf/^{177}Hf$ ratios of the massive quartz monzonite sample (PM2-9–1) from Group II range between 0.282393 and 0.282473, the εHf(t) values range from – 6.9 to – 9.7, and the Hf two-stage modeling ages (T_{DM2}) ranging from 2.27 to 2.52 Ga. The $^{176}Hf/^{177}Hf$ ratios of the Group III porphyritic syenogranite (B0039) vary from 0.282310 to 0.282408, the εHf(t) ranges from − 9.3 to − 12.7, and the Hf two-stage modeling ages (T_{DM2}) range between 2.48 and 2.79 Ga. The Group IV syenogranite sample (PM3-10–2) has initial $^{176}Hf/^{177}Hf$ ratios ranging from 0.282191 to 0.282334, εHf(t) values ranging from −14.4 to −16.9 and Hf two-stage model ages (T_{DM2}) varying from 2.72 to 3.13 Ga.

The results of the whole-rock Sr–Nd isotope analyses are carried out in Supp. 5. The Group III syenogranite (B0039) has $^{87}Rb/^{86}Sr$ ratios ranging from 0.25674 to 0.30110, $^{147}Sm/^{144}Nd$ ratios of 0.0902–0.0911, $^{87}Sr/^{86}Sr$ ratios ranging from 0.70633 to 0.70640, $^{143}Nd/^{144}Nd$ ratios varying from 0.511973 to 0.511974, $(^{87}Sr/^{86}Sr)_i$ values of 0.705686–0.705735, εNd(t) values ranging between − 10.65 and − 10.70 and Nd stage modeling ages (T_{DM}) ranging from 1.58 to 1.59 Ga. The Group IV syenogranite (PM3-10–2) has $^{87}Rb/^{86}Sr$ ratios of 0.30636–0.31502, $^{147}Sm/^{144}Nd$ ratios of 0.0877–0.0889, $^{87}Sr/^{86}Sr$ ratios of 0.70738–0.70740 and $^{143}Nd/^{144}Nd$ values ranging from 0.511842 to 0.511848. $(^{87}Sr/^{86}Sr)_i$ values are 0.706650–0.706653, with εNd(t) values ranging from −13.09 to −13.23 and Nd stage model ages (T_{DM}) between 1.45 and 1.46 Ga.

5 Discussion

5.1 Petrogenesis

Granitoids are generally classified into mantle-derived (M-type), crust-mantle mixing or lower crustal granites (I-type), crustal sediment granites (S-type) and alkaline granites (A-type) (Chappell and White 1992, 2001; Chappell 1999; Eby 1990, 1992; Bonin 2007). These granites can be further categorized by tectonic settings, including mid-ocean ridge granite (ORG), volcanic arc granite (VAG), syn-collisional granite (S-COLG) and intraplate granite (WPG) (Batchelor and Bowden 1985). Additionaly, Defant and Drummoud (1990) subdivided the I-type granites into typical island arc and adakite types. Wu et al. (2003) further distinguished the I-type granites into “undifferentiated” and “highly differentiated” types through theie comprehensive study of Phanerozoic granites in Northeast China.

The geologic and lithologic characteristics of the four groups of granites in the Songjianghe region demonstrate that the rock-forming minerals are predominantly composed of plagioclase, alkali feldspar and quartz, accompanied by melanocratic minerals such as amphibole and biotite, with accessory minerals magnetite, zircon and apatite. This mineral assemblage exhibits a clear correspondence to that of I-type granites (Chappell and White 2001). Geochemical analysis reveals distinct elemental characteristics of the four groups: Group I comprises high-K calc-alkaline and weakly peraluminous series rocks. Group II displays primarily calc-alkaline, sodic and partially high-K calc-alkaline, with metaluminous affinity. Group III is characterized by high-K calc-alkaline, potassic and peraluminous facies. Group IV shows transitional features from high-K calc-alkaline to calc-alkaline, sodic-potassic transition and peraluminous facies. These geochemical characteristics resemble those of I-type granitoids (Chappell and White 2001).

The A/CNK values of Groups I, II and IV range from 0.91 to 1.13, with depletion in Ba, Ti and P indicating I-type granite affinity. Although Group III is slightly enriched in Ba and has the characteristics of A-type granite, the depletion of HFSEs such as Nb, Ta, Ti and Y significantly differs from typical A-type granite (Eby 1990; Bonin 2007). As illustrated in Fig. 7, the compositions of all four groups plot in the undifferentiated or weakly differentiated granite region, while Group I, III and IV approach or overlap the boundary with the highly fractionated granite region (Fig. 7a). On the $(Zr + Nb + Ce + Y)$ vs. $(Na_2O + K_2O)/CaO$ diagram, Group I and II compositions plot in the undifferentiated or weakly differentiated region, whereas Group III and IV compositions straddle the boundary between highly differentiated and undifferentiated granites.

Trace element patterns exhibit characteristics of island-arc granites (Fig. 6), which can be further classified into

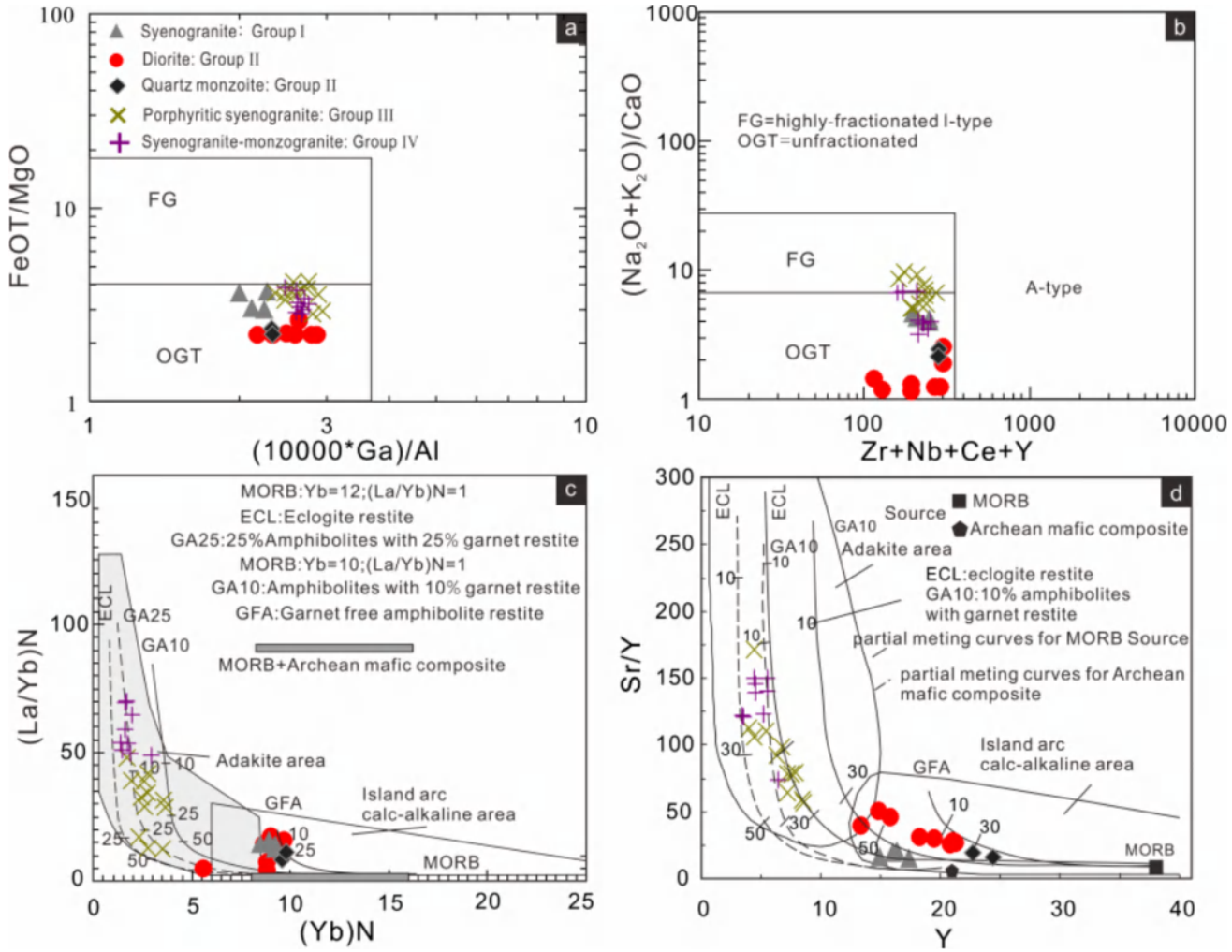

Fig. 7 Discrimination diagrams of **a** FeOT/MgO vs. 10000 Ga/Al (Whalen et al. 1987); **b** $(Na_2O+K_2O)/CaO$ vs. Zr + Nb + Ce + Y (Wu et al. 2003); **c** $(La/Yb)_N$ vs. $(Yb)_N$ (Defant and Drummond 1990a, b); **d** Sr/Y vs. Y (Martin 1999)

typical island arc calc-alkaline granite and adakite granite (Defant and Drummond 1990). On the $(La/Yb)_N$ vs. $(Yb)_N$ and Sr/Y vs. Y diagrams, Groups I and II plot in the typical island arc calc-alkaline granite region adjacent to the adakite region, whereas Groups III and IV plot in the adakite region (Fig. 7c, d). Based on these analyses, Groups I and II are identified as undifferentiated or weakly differentiated, calc-alkaline I-type granites, while Groups III and IV represent differentiated I-type adakite granites.

5.2 Magma origin and evolution

The petrogenesis of the I-type granites has been explained through various mechanisms, which can be summarized as follows: (1) fractional crystallization of mantle-derived basaltic magmas or mixing of crustal and mantle magmas followed by crystallization (AFC process) (Soesoo 2000; Fowler et al. 2008); (2) partial melting of subducting oceanic slabs (Martin et al. 2005); (3) partial melting of ancient crust and juvenile basaltic lower crust (Wu et al. 1998; Han et al. 1998; Hou et al. 2011); (4) partial melting of enriched mantle driven by subduction-derived fluids or metasomatized lithospheric mantle (Wilde 2015; Peng et al. 2016). Based on the elemental and isotopic geochemical charateristics, this paper present distinct features of the four groups of granites in the Songjianghe area.

The Group I granites exhibit Rb/Sr ratios of 0.29–0.41, Nb/Ta ratios of 13.60–23.49 and Lu/Yb values of 0.16–0.17, indicating a lower continental crust origin [e.g., $(Rb/Sr)^{LC}=0.02$, $(Rb/Sr)^{UC}=0.32$, $(Nb/Ta)^{LC}=10$, $(Nb/Ta)^{UC}=11.36$), $(Lu/Yb)^{LC}=0.13$, $(Lu/Yb)^{UC}=0.06$] (Sun and McDonough 1989). The $(La/Yb)_N$ vs. $(Yb)_N$ and the Sr/Y versus Y diagrams suggest a partial melting process involving amphibole with eclogite as a residual mineral (Fig. 7c, d). Negative Eu anomalies indicate that the partial melting residual minerals were dominated by garnet and

amphibole, with minor plagioclase. εHf(t) vs. zircon age (Ma) and $^{176}Hf/^{177}Hf$ vs. zircon age (Ma) diagrams reveal the compositions near the 1.8 Ga crustal evolutionary boundary and the upper limit of the lower crust, suggesting a magma source younger than that of the Archean granitoids (3.0 Ga) in the collage zone. T_{DM2} values of 2.47–2.70 Ga further suggest a Neoarchean lower crust origin, which had been metasomatized by melt or juvenile fluids (Fig. 8e, f). The reducing and water-poor characteristics (Fig. 8a, b) imply that the magma of group I originated from the partial melting of the lower crust that metasomatized by fluids, consistent with its low differentiation degree and the partial melting trends of Groups III and IV (Fig. 10e). Low Nb/La ratios indicate crustal contamination, resulting in lower HFSE/LILE ratios (Rudnick and Gao 2003). Fractional crystallization and assimilation trends are evident on La/Sm vs. La and Nb/La vs. La/Yb diagrams (Fig. 10a, b).

Group II comprises gneiss diorite, granodiorite and massive quartz monzonite; these rocks have Rb/Sr ratios of 0.11–0.35, Nb/Ta ratios of 9.76–15.18 and Lu/Yb ratios of 0.14–0.17, suggesting a lower crust origin. Fe_2O_3/FeO vs. SiO_2 and the Al_2O_3/TiO_2 vs. Sr/Y diagrams indicate reducing and alternately water-poor and weakly water-rich conditons with garnet and amphibole left as remnant minerals (Fig. 7c, d). The compositional points of the quartz monzonite are distributed between the upper boundary of the lower crust and the Paleoarchean crust region at ~ 1.8 Ga, with T_{DM2} ages of 2.27–2.53 Ga. Higher εHf(t) values and T_{DM2} ages than Group I confirm that the magma originated from the Neoarchean lower crust, metasomatized by younger fluids with significant young crustal input during magma evolution (Fig. 8c, e). Furthermore, the εHf(t) values of Group II are relatively similar to Group III, and the Sr–Nd isotopes indicate a predominant lower crustal component (~ 70%) (Fig. 9). Conversely, the magma sources were in relatively reducing and water-poor conditions, with amphibole occurring as a residual mineral during partial melting (Figs. 7, 8). For the gneiss diorite and granodiorite, their compositions exhibit a fraction crystallization trend, while a crustal contamination trend is evident in the Nb/La vs. La/Yb diagram (Fig. 10a, b). Massive quartz monzonite shows lower Nb/La ratios indicating crustal contamination and plots in the active margin environment region (Fig. 10c). Weakly negative Eu anomalies and depletion in HFSEs suggest that amphibole and a minor amount of plagioclase as residual minerals (Figs. 6, 7). Overall, the magma of Group II formed by partial melting of the reduced Neoarchean lower crust (Wu et al. 1999).

The Group III granites show a typical geochemical affinity to the adakites, similar to pre-Cenozoic orogenic belts of igneous rocks (Martin 1999; Zhang et al. 2004; Wang et al. 2006a). Adakitic rocks are classified into high-Ba and high-Sr granites (Tarney and Jones 1994), adakite-like rocks (Harris et al. 1996), "C-type adakites" (Zhang et al. 2001), "crust-derived adakite" (Sheppard et al. 2001), Sr-rich andesite (Conrey et al. 2001) and high-Sr, low-Y intermediate-acidic igneous rocks (Ge et al. 2002; Zeng et al. 2011). Recently, Wang et al. (2020) summarized the geochemical composition and petrogenesis of the adakites at plate convergent margins and concluded that the adakites could be the products of interactions between slab-related melts and the mantle (Kay 1978). Adakites can form by partial melting of the subducted oceanic crust (Defant and Drummoud 1990), delamination of the lower crust (Xu et al. 2002; Gao et al. 2004; Wang et al. 2006b) and subduction of the continental crust (Wang et al. 2007; Jiang et al. 2014) with adakitic melts interacting with the mantle. The Group III granites are low-Mg, alumina-rich, high-silica adakites (Martin et al. 2005), with Rb/Sr ratios of 0.11–0.25, Nb/Ta ratios of 8.90–16.14 and Lu/Yb ratios of 0.14–0.17, indicating a continental crustal source. $(La/Yb)_N$ vs. $(Yb)_N$ and Sr/Y vs. Y diagrams, suggest a 10%–25% degree of partial melting of amphibolites with 25% garnet restite (Fig. 7c, d). εHf(t) versus zircon age (Ma) and $^{176}Hf/^{177}Hf$ versus zircon age (Ma) discrimination diagrams show data points are distributed above the 1.8 Ga crustal evolutionary line near the boundary of the lower crust, with T_{DM2} values of 2.48–2.79 Ga, indicating an Archean lower crust origin that had been metasomatized by younger fluids or melts (Fig. 8). Furthermore, the Sr–Nd isotope compositions suggesta ~ 80% lower crustal contribution (Fig. 9). The source area featured a transitional environment from reducing to oxidizing, with H_2O-containing fluids involved in partial melting (Fig. 8a, b). Weakly positive Eu anomalies indicate partial melting affected alkali feldspar, plagioclase and biotite, with 10 ~ 15% amphibole and garnet as residual minerals (Fig. 7c, d). On the La/Sm vs. La diagram, the data are basically consistent with the partial melting and fractional crystallization trends like those of Groups I and II (Fig. 10a). However, the distribution of composition points shows a distincitve crustal contamination trend (Fig. 10b). Crustal contamination is more prominent than fractional crystallization, evidenced by detrital zircon material in zircon cores (Fig. 4, B0039).

The Group IV granites exhibit strong depletion in HREEs (Yb = 0.29–0.60 ppm, Y = 3.6–6.38 ppm), high Sr contents of 406.57–812.00 ppm, high La/Yb ratios varying from 72.04 to 104.16 and Sr/Y ratios of 120.25–149.71. These values indicate that the studied samples are low-Mg, peraluminous, high-silica adakites (Martin et al. 2005). The Rb/Sr ratios of 0.07–0.20, a mean Nb/Ta ratio of 9.36 and Lu/Yb ratios of 0.15–0.18, suggest a continental lower crust origin. The $(La/Yb)_N$ versus $(Yb)_N$ and Sr/Y versus Y diagrams indicate a 10–15% partial melting of amphibolites with garnet restite (Fig. 7c, d). Additionally, on the εHf(t) vs. zircon age (Ma) and $^{176}Hf/^{177}Hf$ vs. zircon age (Ma) discrimination

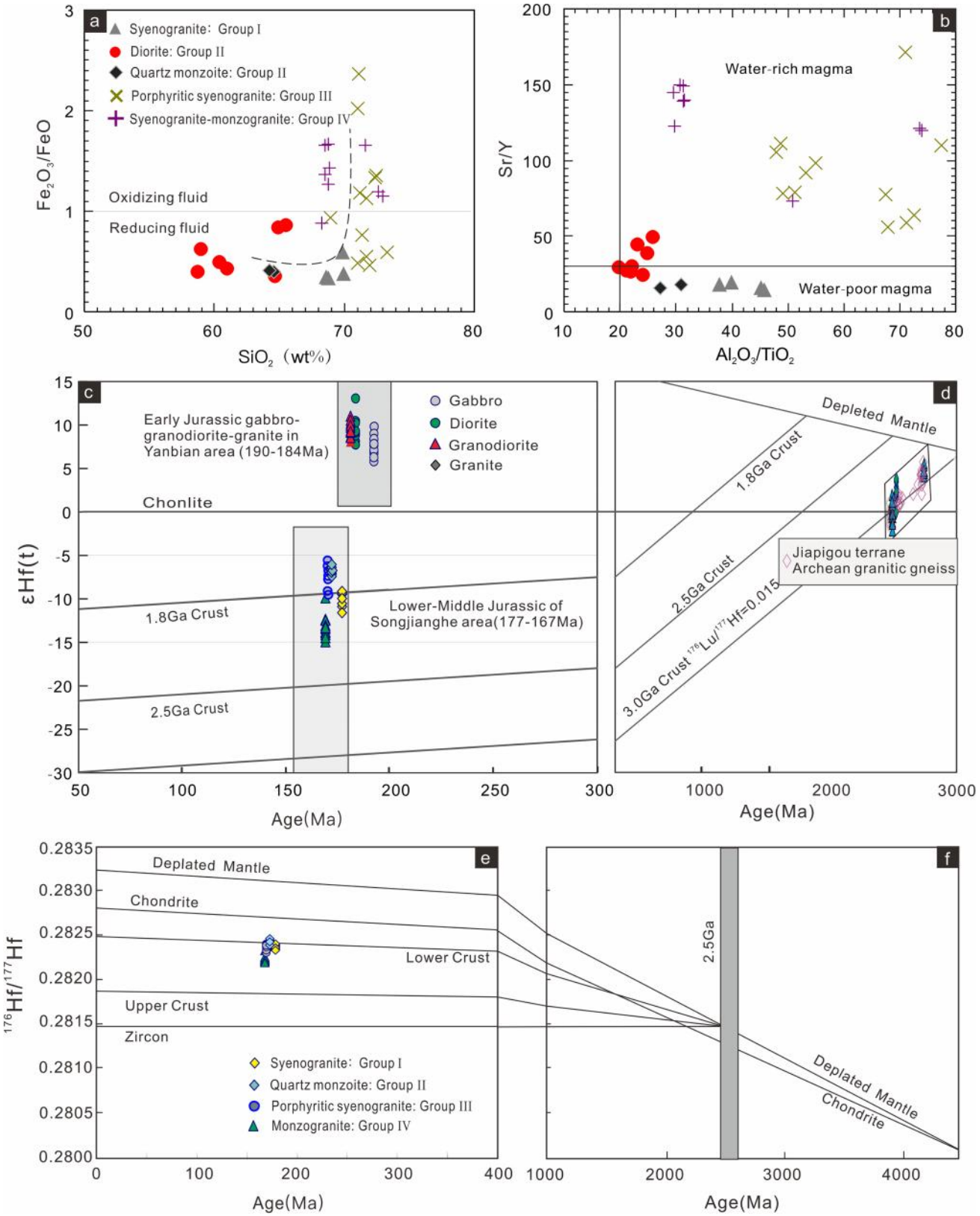

Fig. 8 **a** Fe_2O_3/FeO vs. SiO_2 diagram; **b** Sr/Y vs. Al_2O_3/TiO_2 diagram (Loucks 2014); **c**, **d** εHf(t) vs. zircon age (Ma) diagram (Vervoort et al. 1996); **e**, **f** $^{176}Lu/^{177}Hf$ vs. zircon age (Ma) diagram. The granitoid from the east CAOB and YFTB (data from Yang et al. 2006; Wu et al. 2006). CAOB = the Central Asian Orogenic Belt; YFTB = Yanshan Fold and Thrust Belt

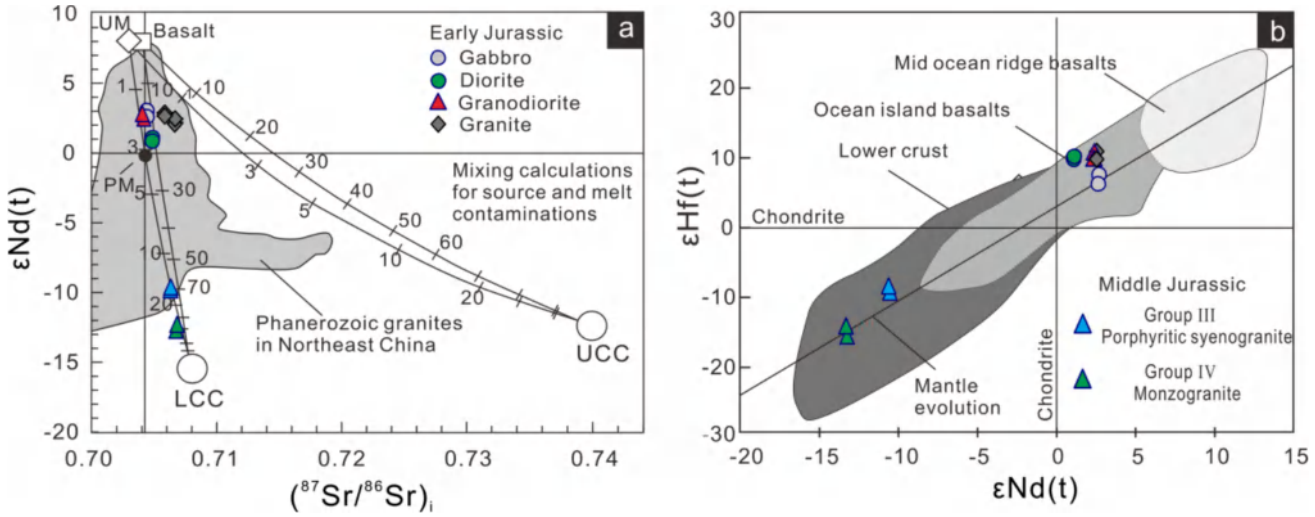

Fig. 9 Discrimination diagrams of Sr–Nd isotopes of Middle Jurassic granites in the study area and Early Jurassic granites in the Yanbian area. **a** εNd(t) vs. ($^{87}Sr/^{86}Sr$)i diagram (Jahn et al.1999); **b** εHf(t) vs. εNd(t) diagram (Dobosi et al. 2003) DM: $^{87}Sr/^{86}Sr = 0.703$,Sr = 20 ppm, $\varepsilon_{Nd} = +8$, Nd = 1.2 ppm. Basalt: $^{87}Sr/^{86}Sr = 0.703$, Sr = 150 ppm, εNd = +8, Nd = 15 ppm. UCC: $^{87}Sr/^{86}Sr = 0.71$, Sr = 350 ppm, εNd = 10, Nd = 26 ppm (Taylor and Mclennan 1985). LCC: $^{87}Sr/^{86}Sr = 0.710$, Sr = 300 ppm, εNd = – 30, Nd = 24 ppm (Rudnick 1995)

diagrams, the compositional points plot in the 1.8–2.5 Ga region with Hf (T_{DM2}) ages of 2.71–3.13 Ga, indicating a middle Archean lower crust or the NCC origin (3.0 Ga). Moreover, the Sr–Nd isotope compositions suggest a Middle Archean lower crust (> 90%) contributon. The magma source was an oxidizing, water-rich environment, reflecting dehydrated partial melting of water-bearing mineral facies, with a mineral facies transition from amphibole to omphacite (Drummond et al. 1996). These conditions are consistent with a low degree of partial melting with eclogite as a residual mineral in the Archean mafic composite source region (Fig. 7d). Furthermore, strong Ba depletion indicates basic plagioclase in the residual minerals. The Nb/La versus La/Yb diagram shows a fractional crystallization evolutionary trend (Fig. 10b). In summary, the magma of Group IV represents a dehydration partial melting of the middle Neoarchean crust accompanied by eclogite facies metamorphism.

In conclusion, the petrogenesis of the four groups of granites in the Songjianghe area indicate that the magma might have originated from the partial melting of Archean lower crust. The magma source conditions of these rocks varied from reducing to oxidizing, with the residual mineral phases ranging from amphibole to eclogite. Crustal contamination significantly influenced the magmatic evolution, except for Group IV.

5.3 Geodynamic and deep geologic processes

U–Pb isotopic analyses of the granitic complex reveal that the magmatism in the Songjianghe region can be chronologically subdivided into two phases: late Early Jurassic (177 Ma) and Middle Jurassic (172–167 Ma). The geochemical compositions of these rocks exhibit remarkable consistency with the characteristics of typical island arc magmas (Fig. 6) (Pearce et al. 1995). From the perspective of regional Mesozoic geotectonic evolution, the study area featured a continental margin environment related to the subduction of the Paleo-Pacific Ocean beneath the Eurasian continent while simultaneously occupying the collage zone between the XMOB and the NCC. Consequently, the Mesozoic magmatic activity demonstrated considerable complexity, maninfesting multiple phases and stages throughout its evolution history (Wu et al. 1998; Wu and Sun, 1999; Han et al. 1998).

Previous investigations of Phanerozoic granites in Northeast China have established that the Early Jurassic (> 172 Ma) magmatism coincided with the subduction of the Paleo-Pacific Plate and subsequent lithospheric delamination, processes that facilitated mantle underplating and partial melting of ancient and juvenile crust. Through petrogenesis of Mesozoic granites in the northern margin of the NCC, researchers have proposed that a significant tectonic transition occurred at 160–150 Ma (Liu et al. 2002; Deng et al. 2009). Furthermore, during the early to mid-Mesozoic prior to 160 Ma, the regional lithosphere remained under a strongly postcollisional thickening environment, characterized by the emplacement of voluminous high-Sr granites with a minor component of peraluminous granites. Based on the petrogenesis of the early Middle Jurassic granites in the southern sector of the Zhang Guangcai Ranges, it can be inferred that the subduction of the Paleo-Pacific Plate

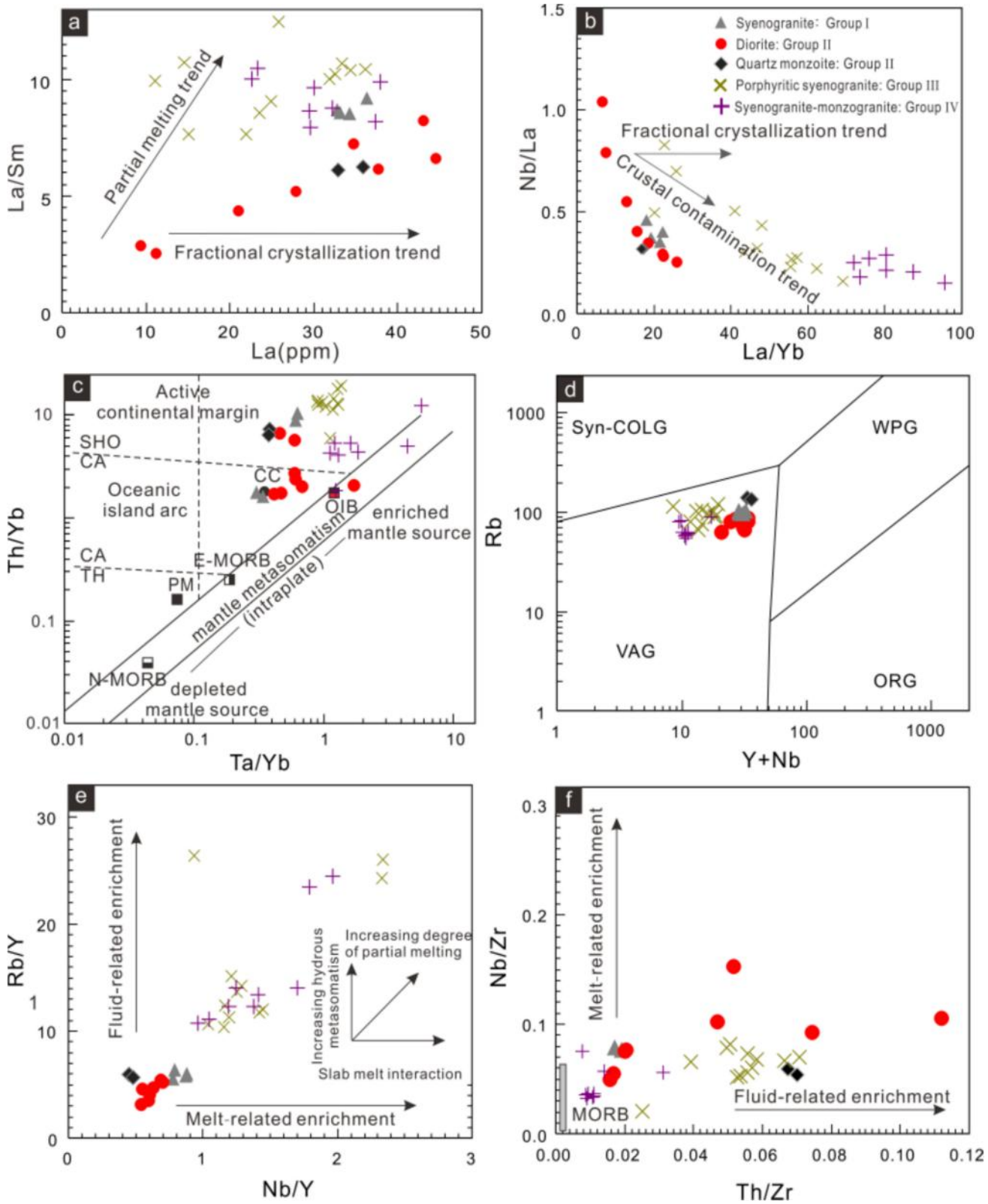

Fig. 10 Discrimination diagrams of the evolution and formation environment of granitic complexes in the study area **a** La/Sm vs. La diagram (Allégre and Minster 1978). **b** Nb/La vs. La/Yb diagram (Rudnick and Gao 2003). **c** Th/Yb vs. Ta/Yb diagram (Pearce 1983; Pearce and Peate 1995). **d** Rb vs. Y + Nb diagram (after Pearce et al. 1984). **e** Rb/Y vs. Nb/Y diagram (after Sajona et al. 1993; Grove et al. 2003). **f** Nb/Zr vs. Th/Zr diagram (after Kepezhinskas et al. 1997)

persisted until the early Middle Jurassic (173 Ma), with the tectonic setting gradually transitioning from a compressional to a postcollisional extensional environment by the late Middle Jurassic (166 Ma) (Ren 2019; Han et al. 2019).

The element and Sr–Nd-Hf isotope geochemical characteristics of the Jurassic granites in the study area provide compelling evidence for magmatism in a typical active continental margin environment (Fig. 10). The magma source was characterized by oceanic fluid metasomatism (Fig. 8e, f) and multistage partial melting processes (Fig. 10a, b). As illustrated in Fig. 11, all samples plot within the superposition region of thick lower crust-derived adakites and subducted oceanic crust-derived adakites. Combined with the features displayed in Fig. 11c and d, these observations indicate that the magmas of Groups I and II formed under medium- to low-pressure conditions, with a discernible pressure increase from Group I to Group II. In constrast, the magmas of Groups III and IV exhibited medium- to high-pressure evolutionary trends.

Based on these findings, we can further conclude that the lower crust of the Songjianghe region experienced compression under medium- to low-pressure conditions at 177 Ma and 172 Ma. These deep geologic processes were driven by the subduction of the Paleo-Pacific Ocean beneath the Eurasian continent, which triggered the crustal thickening and delamination in the Jiapigou-Haigou collage zone, along with partial melting of the reduced Neoarchean lower crust metasomatized by fluid. At 169–167 Ma, the magmas were characterized by medium-high pressure conditions. Partial melting of the thickened Neoarchean lower crust occured

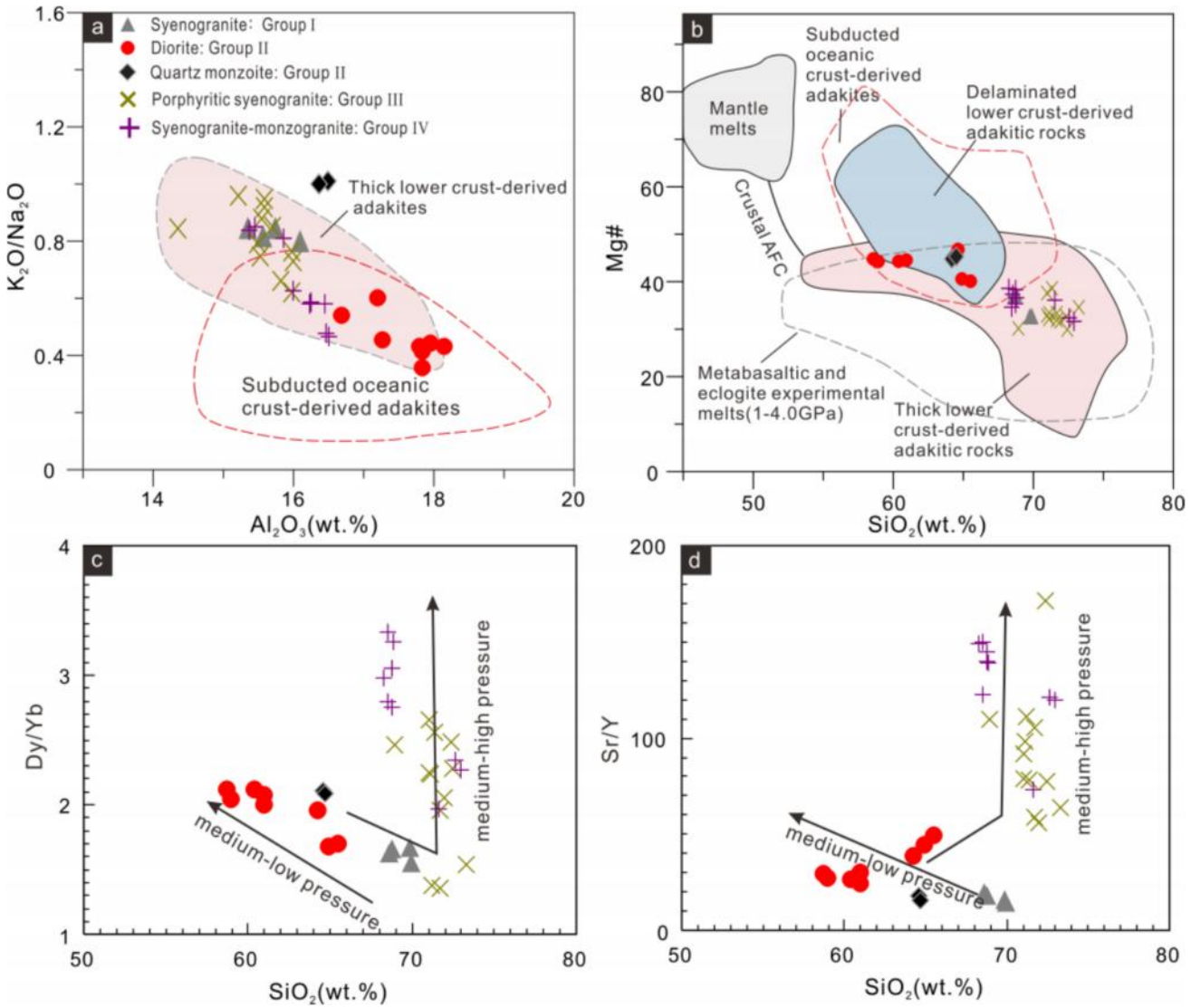

Fig. 11 **a** K_2O/Na_2O vs. Al_2O_3 diagram (Kepezhinskas et al. 1997). **b** Mg# vs. SiO_2 diagram (Wang et al. 2006a, b). **c** Dy/Yb vs. SiO_2 diagram (Defant and Drummond 1990a). **d** Sr/Y vs. SiO_2 diagram (Martin et al. 2005)

under a transition from redox to oxidizing conditions, with the residual mineral phases ranging from amphibole to eclogite. The magmatic evolution process involved fractional crystallization and varying degrees of crustal contamination.

6 Conclusions

Research on zircon U–Pb dating and element geochemistry and Sr–Nd–Hf isotopes of the early-Middle Jurassic granitic complexes in the Songjianghe area of the Jiapigou-Haigou collage zone in northeastern China is presented in this paper. Several conclusions were obtained by discussing the petrogenesis of these rocks and the deep geologic process as follows:

The geochronology investigation and U–Pb isotope dating of the Middle Jurassic rocks in the Songjianghe area ranged from 177 to 167 Ma, providing crucial temporal constraints to help understand the associated magmatic evolution. The granitic complexes can be systematically classified into four distinct lithologic groups based on their compositional characteristics.

The elemental geochemical analysis shows that all four groups of granites belong to the I-type granite series, with specific charateristics as follows: Group I featuring peraluminous, high-K calc-alkaline/potassic, low fractionated I-type granites; Group II featuring metaluminous, calc-alkaline/sodic and a low degree of fractionated I-type granites; Group III featuring peraluminous, high-K calc-alkaline/potassic and relatively highly fractioned I-type adakites; Group IV featuring peraluminous, high-K calc-alkaline, calc-alkaline/potassic-sodic transition and high-K calc-alkaline/potassic, highly differentiated I-type adakites.

The isotopic compositions indicate that the primary magmas of all four groups originated from the dehydrated partial melting of the thickened Neoarchean lower crust under variable reducing to oxidizing conditions. The magmatic evolution involved residual mineral facies transitioning from amphibole to eclogite, accompanied by varying degrees of crustal contamination.

From a regional geodynamic perspective, the deep geologic processes reveal the accretion and delamination of Archean lower crust and the lower crust in the collage zone, triggered by the subduction of the Paleo-Pacific Ocean beneath the Eurasian continent. Large-scale delamination appears to have occurred after < 166 Ma, with the magmatic rocks in the study area showing a predominant affinity with the NCC magmatism.

This research provides significant insights into the tectonic evolution and magmatic processes in the Jiapigou-Haigou collage zone during the Early-Middle Jurassic period, contributing to our further understanding of the complex geodynamic interactions in northeastern China.

Acknowledgements First, we thank the Managing Editor for his patience and tolerance in allowing us to revise the manuscript and two anonymous reviewers for their constructive comments. We sincerely thank Shen Nengping for help with the Sr-Nd isotopic analysis and the State Key Laboratory for Mineral Deposits Research, Nanjing University, for help with zircon Hf isotopic analyses. Sincere thanks are extended to Dr. Keqiang Zhao, Qian Lu, Xiaolei Chu and Xiaotian Zhang for their help.

Author contributions Xinwen Zhang: writting manuscript, analyzing experimental data; Jinggui Sun: advisor, guidance on writing; Zuochao Lin and Shu Wang: analyzing experimental data, sample collection; Yunpeng He: sample collection.

Funding This work was supported by the Natural Science Foundation of Jilin Province of China (grant no. 20230101075JC) and the National Natural Science Foundation of China (grant no. 42072085).

Declarations

Conflict of interest The authors declare there are no competing interests.

References

Allègre CJ, Minster JF (1978) Quantitative models of trace element behavior in magmatic processes. Earth Planet Sci Lett 38(1):1–25. https://doi.org/10.1016/0012-821X(78)90123-1

Batchelor RA, Bowden P (1985) Petrogenetic interpretation of granitoid rock series using multicationic parameters. Chem Geol 48(1–4):43–55. https://doi.org/10.1016/0009-2541(85)90034-8

Belousova E, Griffin W, O'Reilly SY, Fisher N (2002) Igneous zircon: Trace element composition as an indicator of source rock type. Contrib Mineral Petrol 143(5):602–622. https://doi.org/10.1007/s00410-002-0364-7

Bonin B (2007) A-type granites and related rocks: Evolution of a concept, problems and prospects. Lithos 97(1–2):1–29. https://doi.org/10.1016/j.lithos.2006.12.007

Boynton WV (1984) Cosmochemistry of the rare earth elements: Meteorite studies. In Henderson P (ed.) Development in geochemistry. Elsevier, pp 63–114. https://doi.org/10.1016/b978-0-444-42148-7.50008-3

Brown GC, Fyfe WS (1970) The production of granitic melts during ultra-metamorphism. Contrib Mineral Petrol 28(4):310–318. https://doi.org/10.1007/BF00388953

Chappell BW (1999) Aluminium saturation in I- and S-type granites and the characterization of fractionated haplogranites. Lithos 46(3):535–551. https://doi.org/10.1016/S0024-4937(98)00086-3

Chappell BW, White AJR (1992) I- and S-type granites in the Lachlan fold belt. Earth Environ Sci Trans R Soc Edinb 83(1–2):1–26. https://doi.org/10.1017/s0263593300007720

Chappell BW, White AJR (2001) Two contrasting granite types: 25 years later. Aust J Earth Sci 48(4):489–499. https://doi.org/10.1046/j.1440-0952.2001.00882.x

Chen YJ, Sun JG, Ren L, Zhang Y, Men LJ (2013) Petrogenesis of the Wudaogou intermediate–mafic complex, NW China: Zircon U-Pb dating, whole-rock and isotope geochemistry, and geological

implications. Int Geol Rev 55(16):1959–1977. https://doi.org/10.1080/00206814.2013.810373

Conrey RM, Hooper PR, Larson PB, Chesley J, Ruiz J (2001) Trace element and isotopic evidence for two types of crustal melting beneath a high cascade volcanic center, Mt. Jefferson Oregon. Contrib Mineral Petrol 141(6):710–732. https://doi.org/10.1007/s004100100259

Defant MJ, Drummond MS (1990) Derivation of some modern arc magmas by melting of young subducted lithosphere. Nature 347:662–665. https://doi.org/10.1038/347662a0

Deng J, Yang LQ, Gao BF, Sun ZS, Guo CY, Wang QF, Wang JP (2009) Fluid evolution and metallogenic dynamics during tectonic regime transition: Example from the Jiapigou gold belt in Northeast China. Resour Geol 59(2):140–152. https://doi.org/10.1111/j.1751-3928.2009.00086.x

Deng J, Yuan WM, Carranza EJM, Yang LQ, Wang CM, Yang LY, Hao NN (2014) Geochronology and thermochronometry of the Jiapigou gold belt, northeastern China: New evidence for multiple episodes of mineralization. J Asian Earth Sci 89:10–27. https://doi.org/10.1016/j.jseaes.2014.03.013

DePaolo DJ, Perry FV, Baldridge WS (1992) Crustal versus mantle sources of granitic magmas: a two-parameter model based on Nd isotopic studies. Earth Environ Sci Trans R Soc Edinb 83(1–2):439–446. https://doi.org/10.1017/s0263593300008117

Dobosi G, Kempton PD, Downes H, Embey-Isztin A, Thirlwall M, Greenwood P (2003) Lower crustal granulite xenoliths from the Pannonian Basin, Hungary, part 2: Sr–Nd–Pb–Hf and O isotope evidence for formation of continental lower crust by tectonic emplacement of oceanic crust. Contrib Mineral Petrol 144(6):671–683. https://doi.org/10.1007/s00410-002-0422-1

Drummond MS, Defant MJ, Kepezhinskas PK (1996) Petrogenesis of slab-derived trondhjemite–tonalite–dacite/adakite magmas. Earth Environ Sci Trans R Soc Edinb 87(1–2):205–215. https://doi.org/10.1017/s0263593300006611

Eby GN (1990) The A-type granitoids: a review of their occurrence and chemical characteristics and speculations on their petrogenesis. Lithos 26(1–2):115–134. https://doi.org/10.1016/0024-4937(90)90043-Z

Eby GN (1992) Chemical subdivision of the A-type granitoids: petrogenetic and tectonic implications. Geology 20(7):641. https://doi.org/10.1130/0091-7613(1992)020%3c0641

Ewart A (1982) The mineralogy and petrology of Tertiary-recent orogenic volcanic rocks: with special reference to the andesitic-basaltic compositional range. In: Thorp RS (ed) Andesites: orogenic andesites and related rocks. John Wiley and Sons, New York, pp 25–95

Fowler MB, Kocks H, Darbyshire DPF, Greenwood PB (2008) Petrogenesis of high Ba–Sr plutons from the northern Highlands terrane of the British Caledonian Province. Lithos 105(1–2):129–148. https://doi.org/10.1016/j.lithos.2008.03.003

Gao S, Rudnick RL, Yuan HL, Liu XM, Liu YS, Xu WL, Ling WL, Ayers J, Wang XC, Wang QH (2004) Recycling lower continental crust in the North China Craton. Nature 432(7019):892–897. https://doi.org/10.1038/nature03162

Ge XY, Li XH, Chen ZG, Li WP (2002) Geochemistry and petrogenesis of Jurassic high Sr/low Y granitoids in eastern China: constrains on crustal thickness. Chin Sci Bull 47(11):962–968. https://doi.org/10.1360/02tb9216

Griffin WL, Pearson NJ, Belousova E, Jackson SE, van Achterbergh E, O'Reilly SY, Shee SR (2000) The Hf isotope composition of cratonic mantle: LAM-MC-ICPMS analysis of zircon megacrysts in kimberlites. Geochim Cosmochim Acta 64(1):133–147. https://doi.org/10.1016/S0016-7037(99)00343-9

Griffin WL, Wang X, Jackson SE, Pearson NJ, O'Reilly SY, Xu XS, Zhou XM (2002) Zircon chemistry and magma mixing, SE China: *in situ* analysis of Hf isotopes. Tonglu Pingtan Igneous Complexes Lithos 61(3–4):237–269. https://doi.org/10.1016/S0024-4937(02)00082-8

Grove TL, Elkins-Tanton LT, Parman SW, Chatterjee N, Müntener O, Gaetani GA (2003) Fractional crystallization and mantle-melting controls on calc-alkaline differentiation trends. Contrib Mineral Petrol 145(5):515–533. https://doi.org/10.1007/s00410-003-0448-z

Hamilton AJS, Sarazin CL, Chevalier RA (1983) Astrophys J Sup Ser 51:115

Han BF, He GQ, Wang SG, Hong DW (1998) Postcollisional mantle-derived magmatism and vertical growth of the continental crust in north Xinjiang. Geol Rev 44(4):396–406. https://doi.org/10.16509/j.georeview.1998.04.009. (**in Chinese with English abstract**)

Han JL, Sun JG, Liu Y, Ren L, Wang CS, Zhang XT, He YP, Yu RD, Lu Q (2019) Jurassic granitic magmatism in the lesser Xing'an-Zhangguangcai ranges of NE China: the Dong'an example. Int Geol Rev 61(17):2143–2163. https://doi.org/10.1080/00206814.2019.1581998

Han JL, Deng J, Zhang Y, Sun JG, Wang QF, Zhang YM, Zhang XT, Liu Y, Zhao CT, Yang F, Wang LL, Lin ZC (2022) Au mineralization-related magmatism in the giant Jiapigou mining district of northeast China. Ore Geol Rev 141:104638. https://doi.org/10.1016/j.oregeorev.2021.104638

Harris NR, Sisson VB, Wright JE, Pavlis TL (1996) Evidence for eocene mafic underplating during fore-arc intrusive activity, eastern Chugach mountains. Alaska Geol 24(3):263. https://doi.org/10.1130/0091-7613(1996)024%3c0263:efemud%3e2.3.co;2

Liu HT, Zhai MG, Liu JM, Sun SH(2002) The Mesozoic granitoids in the northern marginal region of North China Craton: evolution from post-collisional to ano rogenic settings. Acta Petrologica Sinica 18: 433–448.

Hou ZQ, Zhang HR, Pan XF, Yang ZM (2011) Porphyry Cu(–Mo–Au) deposits related to melting of thickened mafic lower crust: examples from the eastern tethyan metallogenic domain. Ore Geol Rev 39(1–2):21–45. https://doi.org/10.1016/j.oregeorev.2010.09.002

Jahn BM, Wu FY, Lo CH, Tsai CH (1999) Crust–mantle interaction induced by deep subduction of the continental crust: geochemical and Sr–Nd isotopic evidence from post-collisional mafic–ultramafic intrusions of the northern Dabie complex. Central China Chem Geol 157(1–2):119–146. https://doi.org/10.1016/S0009-2541(98)00197-1

Jiang ZQ, Wang Q, Wyman DA, Li ZX, Yang JH, Shi XB, Ma L, Tang GJ, Gou GN, Jia XH, Guo HF (2014) Transition from oceanic to continental lithosphere subduction in southern Tibet: evidence from the Late Cretaceous-Early Oligocene (~91–30 Ma) intrusive rocks in the Chanang-Zedong area, southern Gangdese. Lithos 196–197:213–231. https://doi.org/10.1016/j.lithos.2014.03.001

Kay RW (1978) Aleutian magnesian andesites: Melts from subducted Pacific ocean crust. J Volcanol Geotherm Res 4(1-2):117-132.

Kepezhinskas P, McDermott F, Defant MJ, Hochstaedter A, Drummond MS, Hawkesworth CJ, Koloskov A, Maury RC, Bellon H (1997) Trace element and Sr–Nd–Pb isotopic constraints on a three-component model of Kamchatka Arc petrogenesis. Geochim Cosmochim Acta 61(3):577–600. https://doi.org/10.1016/s0016-7037(96)00349-3

Li L, Sun JG, Men LJ, Chai P (2017) Genesis of the Haigou gold deposit, Jilin Province, NE China: evidence from fluid inclusions, $^{40}Ar/^{39}Ar$ geochronology and isotopes. Geol J 52(6):992–1008. https://doi.org/10.1002/gj.2864

Liang HD, Gao R, Hou HS, Li WH, Han JT, Liu GX, Han S (2015) Post-collisional extend record at crustal scale: revealed by the deep electrical structure from the southern margin of the Central Asian Orogenic Belt to the northern margin of the North China Craton. Chin J Geol Sci Geol Sin 50(2):643–652 (**in Chinese with English abstract**)

Liégeois JP, Navez J, Hertogen J, Black R (1998) Contrasting origin of post-collisional high-K calc-alkaline and shoshonitic versus alkaline and peralkaline granitoids. Use Sliding Normalization Lithos 45(1–4):1–28. https://doi.org/10.1016/S0024-4937(98)00023-1

Liu WG, Li ZD, Wei S, Chen J, Liu Y, Ao C, Xiao ZB, Zhou HY, Liu H (2019) Rapid separation and precise determination of strontium isotopic from geological samples with high rubidium/strontium ratios. Chin J Anal Chem 47(7):1054–1060. https://doi.org/10.1016/S1872-2040(19)61172-2

Loucks RR (2014) Distinctive composition of copper-ore-forming arcmagmas. Aust J Earth Sci 61(1):5–16. https://doi.org/10.1080/08120099.2013.865676

Maniar PD, Piccoli PM (1989) Tectonic discrimination of granitoids. Geol Soc Am Bull 101(5):635–643. https://doi.org/10.1130/0016-7606(1989)1010635:tdog%3e2.3.co;2

Martin H (1999) Adakitic magmas: modern analogues of archaean granitoids. Lithos 46(3):411–429. https://doi.org/10.1016/S0024-4937(98)00076-0

Martin H, Smithies RH, Rapp R, Moyen JF, Champion D (2005) An overview of adakite, tonalite–trondhjemite–granodiorite (TTG), and sanukitoid: relationships and some implications for crustal evolution. Lithos 79(1–2):1–24. https://doi.org/10.1016/j.lithos.2004.04.048

Middlemost EAK (1994) Naming materials in the magma/igneous rock system. Earth Sci Rev 37(3–4):215–224. https://doi.org/10.1016/0012-8252(94)90029-9

Nowell GM, Kempton PD, Noble SR, Fitton JG, Saunders AD, Mahoney JJ, Taylor RN (1998) High precision Hf isotope measurements of MORB and OIB by thermal ionisation mass spectrometry: insights into the depleted mantle. Chem Geol 149(3–4):211–233. https://doi.org/10.1016/S0009-2541(98)00036-9

Pearce J, Peate DW (1995) Tectonic implications of the composition of volcanic arc magmas. Annu Rev Earth Planet Sci 23:251–285. https://doi.org/10.1146/annurev.earth.23.1.251

Pearce JA, Harris NBW, Tindle AG (1984) Trace element discrimination diagrams for the tectonic interpretation of granitic rocks. J Petrol 25(4):956–983. https://doi.org/10.1093/petrology/25.4.956

Pearce J (1983) Role of the sub-continental lithosphere in magma genesis at active continental margins. In (Hawkeswrth CJ, Norry MJ eds) Continental basalts and mantle xenoliths: Nantwich, Shiva pp. 230–249

Peccerillo A, Taylor SR (1976) Geochemistry of eocene calc-alkaline volcanic rocks from the Kastamonu area. Northern Turkey Contrib Mineral Petrol 58(1):63–81. https://doi.org/10.1007/BF00384745

Peng C, Xue LF, Zhu M, Chai Y, Liu WY (2016) The location and evolution of the tectonic boundary between the Paleoproterozoic Jiao-Liao-Ji Belt and the Longgang Block, northeast China. Precambrian Res 272:18–38. https://doi.org/10.1016/j.precamres.2015.10.016

Pitcher WS (1997) The nature and origin of granite. Chapman & Hall, London. https://doi.org/10.1180/minmag.1998.062.2.01

Ren YJ (2019) Early-middle Jurassic granitic magmatism and tectonic evolution in the southern part of Zhangguangcailing. Acta Ueologica Sinica 93:2813–2831 (**in Chinese with English abstract**)

Rudnick RL (1995) Making continental crust. Nature 378(6557):571–578. https://doi.org/10.1038/378571a0

Rudnick RL, Gao S (2003) Composition of the continental crust. In (Rudnick RL ed) Treatise on Geochemistry. Elsevier. pp 1–64. https://doi.org/10.1016/b0-08-043751-6/03016-4

Sajona FG, Maury RC, Bellon H, Cotten J, Defant MJ, Pubellier M (1993) Initiation of subduction and the generation of slab melts in western and eastern Mindanao, Philippines. Geology 21(11):1007. https://doi.org/10.1130/0091-7613(1993)021%3c1007:iosatg%3e2.3.co;2

Scherer E, Munker C, Mezger K (2001) Calibration of the lutetium-hafnium clock. Science 293(5530):683–687. https://doi.org/10.1126/science.1061372

Sheppard SMF, Harris C (1985) Hydrogen and oxygen isotope geochemistry of Ascension Island lavas and granites: Variationwith crystal fractionation and interaction with sea water. Contrib Mineral Petrol 91:74–81.

Soesoo A (2000) Fractional crystallization of mantle-derived melts as a mechanism for some I-type granite petrogenesis: an example from Lachlan Fold Belt. Australia J Geol Soc 157(1):135–149. https://doi.org/10.1144/jgs.157.1.135

Sun SS, McDonough WF (1989) Chemical and isotopic systematics of oceanic basalts: implications for mantle composition and processes. In: (Saunders AD, Norry MJ eds.) magmatism in ocean basins. Geol Soc Lond Spec Publ 42(1):313–345. https://doi.org/10.1144/gsl.sp.1989.042.01.19

Sun JG, Chen L, Zhao JK, Men LJ, Pang W, Chen D, Liang SN (2008) SHRIMP U-Pb dating of zircons from late Yanshanian granitic complex in Xiaoxinancha gold-rich copper orefield of Yanbian and its geological implications. Miner Depos 27(3):319–328 (**in Chinese with English abstract**)

Sun JG, Zhang Y, Xing SW, Zhao KQ, Zhang ZJ, Bai LA, Ma YB, Liu YS (2012) Genetic types, ore-forming age and geodynamic setting of endogenic molybdenum deposits in the eastern edge of Xing-Meng orogenic belt. Acta Petrol Sin 28(4):1317–1332 (**in Chinese with English abstract**)

Sun JG, Zhang Y, Han SJ, Men LJ, Li YX, Chai P, Yang F (2013) Timing of formation and geological setting of low-sulphidation epithermal gold deposits in the continental margin of NE China. Int Geol Rev 55(5):608–632. https://doi.org/10.1080/00206814.2012.729658

Sylvester PJ (1998) Post-collisional strongly peraluminous granites. Lithos 45(1–4):29–44. https://doi.org/10.1016/s0024-4937(98)00024-3

Tarney J, Jones CE (1994) Trace element geochemistry of orogenic igneous rocks and crustal growth models. J Geol Soc 151(5):855–868. https://doi.org/10.1144/gsjgs.151.5.0855

Taylor SR, Mclennan SM (1985) The continental crust: Its composition and evolution. Blackwell, Oxford

Vervoort JD, Patchett PJ, Gehrels GE, Nutman AP (1996) Constraints on early earth differentiation from hafnium and neodymium isotopes. Nature 379:624–627. https://doi.org/10.1038/379624a0

Wang Q, Xu JF, Jian P, Bao ZW, Zhao ZH, Li CF, Xiong XL, Ma JL (2006a) Petrogenesis of adakitic porphyries in an extensional tectonic setting, Dexing, South China: implications for the genesis of porphyry copper mineralization. J Petrol 47(1):119–144

Wang Q, Wyman DA, Xu JF, Zhao ZH, Jian P, Xiong XL, Bao ZW, Li CF, Bai ZH (2006b) Petrogenesis of cretaceous adakitic and shoshonitic igneous rocks in the Luzong area, Anhui Province (eastern China): implications for geodynamics and Cu–Au mineralization. Lithos 89(3–4):424–446. https://doi.org/10.1016/j.lithos.2005.12.010

Wang T, Wang XX, Zheng YD, Hong DW, Wang XS (2007) Studies on structures of granitic plutons and granitic tectonic dynamics. Chin J Geol Sci Geol Sin 42(1):91–113 (**in Chinese with English abstract**)

Wang Q, Hao LL, Zhang XZ, Zhou JS, Wang J, Li QW, Ma L (2020) Adakitic rocks at convergent plate boundaries: Compositions and petrogenesis. J Earth Sci (English edn) 12:1992-2016.

Whalen JB, Currie KL, Chappell BW (1987) A-type granites: geochemical characteristics, discrimination and petrogenesis. Contrib Mineral Petrol 95(4):407–419. https://doi.org/10.1007/BF00402202

Wilde SA (2015) Final amalgamation of the Central Asian orogenic belt in NE China: Paleo-Asian Ocean closure versus paleo-Pacific plate subduction: a review of the evidence. Tectonophysics 662:345–362. https://doi.org/10.1016/j.tecto.2015.05.006

Whitney G, Northrop RH (1988) Experimental investigation of the smectite to illite reaction; dual reaction mechanisms and oxygen-isotope systematics. Ame Mineral 73(1-2):77-90.

Woodhead JD, Hergt JM (2005) A preliminary appraisal of seven natural zircon reference materials for *In situ* Hf isotope determination. Geostandard Geoanalytic Res 29(2):183–195. https://doi.org/10.1111/j.1751-908x.2005.tb00891.x

Wu FY, Sun DY (1999) The Mesozoic magmatism and lithospheric thinning in Eastern China. J Changchun Univ Sci Technol 29(4):313–318. https://doi.org/10.13278/j.cnki.jjuese.1999.04.001 (**in Chinese with English abstract**)

Wu FY, Jahn B, Lin Q (1998) Isotopic characteristics of the postorogenic granites in orogenic belt of northern China and their implications in crustal growth. Chin Sci Bull 43(5):420–424. https://doi.org/10.1007/BF02883724

Wu FY, Sun DY, Lin Q (1999) Genesis and crustal proliferation of Phanerozoic granite in NorthEast China. Acta Petrol Sin 15(2):181–189 (**in Chinese with English abstract**)

Wu FY, Jahn BM, Wilde SA, Lo CH, Yui TF, Lin Q, Ge WC, Sun DY (2003) Highly fractionated I-type granites in NE China (I): geochronology and petrogenesis. Lithos 66(3–4):241–273. https://doi.org/10.1016/S0024-4937(02)00222-0

Wu FY, Yang YH, Xie LW, Yang JH, Xu P (2006) Hf isotopic compositions of the standard zircons and baddeleyites used in U-Pb geochronology. Chem Geol 234(1–2):105–126. https://doi.org/10.1016/j.chemgeo.2006.05.003

Wu FY, Sun DY, Ge WC, Zhang YB, Grant ML, Wilde SA, Jahn BM (2011) Geochronology of the phanerozoic granitoids in northeastern China. J Asian Earth Sci 41(1):1–30. https://doi.org/10.1016/j.jseaes.2010.11.014

Xu JF, Shinjo R, Defant MJ, Wang Q, Rapp RP (2002) Origin of mesozoic adakitic intrusive rocks in the Ningzhen area of East China: partial melting of delaminated lower continental crust? Geology 30(12):1111. https://doi.org/10.1130/0091-7613(2002)030%3c1111:oomair%3e2.0.co;2

Yang J, Wu F, Shao J, Wilde S, Xie L, Liu X (2006) Constraints on the timing of uplift of the Yanshan fold and thrust belt, North China. Earth Planet Sci Lett 246(3–4):336–352. https://doi.org/10.1016/j.epsl.2006.04.029

Yang DG, Sun DY, Hou XG, Mao AQ, Tang ZY, Qin Z (2018) Geochemistry and zircon Hf isotopes of the early mesozoic intrusive rocks in the south Hunchun, Yanbian area, Northeast China: petrogenesis and implications for crustal growth. Int Geol Rev 60(8):1038–1060. https://doi.org/10.1080/00206814.2017.1365019

Yu RD, Sun JG, Wang S, Han JL, Liu Y (2021) Neoarchean–early paleoproterozoic crustal evolution in the Jiapigou terrane in the northeastern part of the North China Craton: Geochemistry, zircon U-Pb dating and Hf isotope constraints from the potassic granitic complex. Precambrian Res 364:106341. https://doi.org/10.1016/j.precamres.2021.106341

Zeng LS, Gao L, Xie KJ, Jing LZ (2011) Mid-eocene high Sr/Y granites in the northern Himalayan gneiss domes: melting thickened lower continental crust. Earth Planet Sci Lett 303(3–4):251–266. https://doi.org/10.1016/j.epsl.2011.01.005

Zhang Q, Wang Y, Qian Q, Yang JH, Wang YL, Zhao TP, Guo GJ (2001) The characteristics and tectonic-metallogenic significances of the adakites in Yanshan period from eastern China. Acta Petrologica Sinica 17:236–244 (**in Chinese with English abstract**)

Zhang YB, Wu FY, Li HM, Lu XP, Sun DY, Zhou HY (2002) Single grain zircon U-Pb ages of the Huangniling granite in Jilin province. Acta Petrol Sin 18(4):475–481 (**in Chinese with English abstract**)

Zhang YB, Wu FY, Wilde SA, Zhai MG, Lu XP, Sun DY (2004) Zircon U-Pb ages and tectonic implications of 'Early Paleozoic' granitoids at Yanbian, Jilin province. Northeast China Isl Arc 13(4):484–505. https://doi.org/10.1111/j.1440-1738.2004.00442.x

Zhang XT, Sun JG, Yu ZT, Song QH (2019) LA-ICP-MS zircon U-Pb and sericite $^{40}Ar/^{39}Ar$ ages of the Songjianghe gold deposit in southeastern Jilin Province, Northeast China, and their geological significance. Can J Earth Sci 56(6):607–628. https://doi.org/10.1139/cjes-2018-0254

Zhang XW, Sun JG, Xu ZK, Liu Y, Zhao CT (2023) Petrogenesis and geochemical evidence from Early Jurassic intrusive rocks and their implications for subduction of the Paleo-Pacific Plate in the Yanbian area. NorthEast China Can J Earth Sci 60(9):1327–1348. https://doi.org/10.1139/cjes-2022-0119